PROBING THE LOCAL BUBBLE WITH DIFFUSE INTERSTELLAR BANDS. II.
THE DIB PROPERTIES IN THE NORTHERN HEMISPHERE

Amin Farhang[1,2], Habib G. Khosroshahi[1], Atefeh Javadi[1], Jacco Th. van Loon[3],
Mandy Bailey[3], Alireza Molaeinezhad[1], Saeed Tavasoli[1], Farhang Habibi[1],
Ehsan Kourkchi[1,4], Sara Rezaei[1], Maryam Saberi[1], and Liam Hardy[5]

[1] School of Astronomy, Institute for Research in Fundamental Sciences (IPM), PO Box 19395-5746 Tehran, Iran; a.farhang@ipm.ir
[2] Department of Physics, Sharif University of Technology, PO Box 11365-9161 Tehran, Iran
[3] Astrophysics Group, Lennard-Jones Laboratories, Keele University, Staffordshire ST5 5BG, UK
[4] Institute for Astronomy, University of Hawaii, 2680 Woodlawn Drive, HI 96822, USA
[5] Isaac Newton Group, Apartado 321, E-38700 Santa Cruz de La Palma, Spain

ABSTRACT

We present a new high signal-to-noise ratio spectroscopic survey of the Northern hemisphere to probe the Local Bubble and its surroundings using the $\lambda 5780$ Å and $\lambda 5797$ Å diffuse interstellar bands (DIBs). We observed 432 sightlines to a distance of 200 pc over a duration of three years. In this study, we establish the $\lambda 5780$ and $\lambda 5797$ correlations with Na I, Ca II and E_{B-V}, for both inside and outside the Local Bubble. The correlations show that among all neutral and ionized atoms, the correlation between Ca II and $\lambda 5780$ is stronger than its correlation with $\lambda 5797$, suggesting that $\lambda 5780$ is more associated with regions where Ca^+ is more abundant. We study the $\lambda 5780$ correlation with $\lambda 5797$, which shows a tight correlation within and outside the Local Bubble. In addition, we investigate the DIB properties in UV irradiated and UV shielded regions. We find that, within and beyond the Local Bubble, $\lambda 5797$ is located in denser parts of clouds, protected from UV irradiation, while $\lambda 5780$ is located in the low-density regions of clouds.

Key words: ISM: abundances – ISM: bubbles – ISM: clouds – ISM: lines and bands – stars: atmospheres

1. INTRODUCTION

We are living inside a region within the Milky Way disk with extremely low neutral gas densities $n(H) \sim 0.01$ cm^{-3} (Bohlin 1975; Weaver et al. 1977) and purportedly hot temperature ($T \sim 10^6$ K, for more discussion see Welsh & Shelton (2009)). This high temperature was derived based on the distribution of diffuse soft X-ray background emission (Snowden et al. 1998). This large cavity is known as the Local Bubble (LB) or the Local Cavity (Paresce 1984). The evidence that led to the recognition of the Local Bubble comprises (1) the lack of spectral hardening in the observed soft X-ray background that requires low values of neutral gas absorption (Bowyer et al. 1968), (2) low values of interstellar extinction measured for stars within a distance of $\sim$100 pc, as compared with the extinction in sightlines of more distant regions in the interstellar medium (ISM) (Fitzgerald 1968), and (3) observations of Lyα absorption of nearby stars and H I column densities, measured by Bohlin (1975), which showed that this region has a low density.

Most of the theoretical models of the Local Bubble formation favor the production of highly ionized atoms in collisional ionization equilibrium at a conductive interstellar cloud interface (Slavin 1989). High spectral resolution observations have revealed many small and partially ionized Ca II gas clouds (local fluff) within 30 pc (Crawford 2001), thus we expect a significant number of such fluffs at larger distances along sightlines through the Local Bubble. Therefore, the distribution of hot gas remains unresolved.

According to recent observations of neutral (Na I) and ionized (Ca II) atoms, the Local Bubble is extended to a distance of $\sim$80 pc in the Galactic plane and up to hundreds of parsecs into the Halo (Vergely et al. 2001; Lallement et al. 2003; Welsh et al. 2010). Also, three-dimensional (3D) gas maps around the Local Bubble reveal that this cavity has a chimney-like structure

with a narrow opening toward the north Galactic pole (tilted at $l \sim 180°$ and $b \sim +75°$) and a wider opening in the Southern hemisphere (Welsh et al. 2010). Since the Local Bubble and most surrounding cavities are supposedly filled with hot gas densities, such 3D distributions have been studied with diffuse X-ray background emissions to compare the morphology of the nearby cavities with the soft X-ray data (Puspitarini et al. 2014).

The origin of the Local Bubble is still unknown. Crawford (1991) found that the majority of the absorptions toward stars in the Sco–Cen association (170 pc) have negative radial velocities relative to the Local Standard of Rest (LSR). Therefore, most of the diffuse clouds in this direction are moving away from the Sco–Cen association and are approaching us. Currently, the most plausible model is that the Local Bubble has been created by a number of successive supernovae in the nearby Sco–Cen association. Smith et al. (2001) inspected one-dimensional multiple explosion models and found that this scenario requires two to three supernovae to have occurred in the general vicinity of the Sun within the last few million years (probably two to five million years ago).

We initiated a high signal-to-noise spectroscopic survey to map the Local Bubble through absorption in diffuse interstellar bands (DIBs). ISM maps of DIBs have been created in the recent past, toward the globular clusters ω Centauri (van Loon et al. 2009) and the Tarantula Nebula in the Large Magellanic Cloud (van Loon et al. 2013). Also, the pseudo 3D map of the 8620 Å DIB within 3 kpc from the Sun has been produced (Kos et al. 2014). In the first paper in this series (Bailey et al. 2015), we present the results from the southern hemisphere survey. In this paper, we present the results from the northern hemisphere survey. Our aim is to (1) investigate the DIB distribution within and outside of the Local Bubble and (2) examine the DIB correlations with atomic and ionized species in this region. We begin with a brief discussion in Section 2 of the

history and the properties of DIBs. In Section 3, we present the technical aspects of the study, observations, and the target selection. In Section 4, we present the data analysis procedures. In the next three sections, we discuss the results of various DIB properties inside and outside the Local Bubble, according to their Equivalent Widths (EWs), correlations, and UV sensitivity. Finally, in Section 8, we summarize the implications of our results.

2. DIFFUSE INTERSTELLAR BANDS

Observing the first DIBs, in the spectra of reddened stars, by Heger (1922) was the starting point to the oldest puzzle in stellar spectroscopy that still remains unresolved. While Heger argued that DIBs are stellar, more than a decade later Merrill (1936) argued for the interstellar nature of DIBs. At the present, the DIBs are known to comprise ∼500 narrow to broad interstellar absorption features, which are observed ubiquitously between 4000 and 10000 Å (Herbig 1995).

DIBs are studied toward specific targets or large numbers of stars. Hobbs et al. (2009, 2008) carried out a complete survey of HD 204827 and HD 183143 to investigate very weak and relatively narrow bands with typical EWs down to a few mÅ. Over the last decade, many astronomical and laboratory experiments have been accomplished to find and understand DIB carriers as well as a number of theoretical studies. Based on these studies, DIB candidates could be among an infinite number of large carbon-based "organic" molecules (Sarre 2006). To extract physical information about DIB carriers, some correlation studies have been done: (1) DIB correlations with atomic and molecular interstellar species, for instance many studies have considered the λ5780 Å and λ5797 Å DIBs correlation with H I, H_2, Na I D lines, Ca I (4227.9 Å), Ca II (3934.8 Å), K I, CH (4300.3 Å), CH^+ (4232.3 Å), CN (3874.6 Å), and Ti II (Herbig 1995; Weselak et al. 2008), (2) DIB correlations with extinction E_{B-V} (Vos et al. 2011), and (3) DIB correlations with other DIB absorptions (see Vos et al. 2011; Friedman et al. 2011; Kos & Zwitter 2013).

DIBs are used for different purposes in astronomy. For instance, the most outstanding DIBs in the optical waveband; λ4429, λ5780, and λ5797 are empirically known to trace the neutral phase of the ISM. The strength of these DIBs is correlated with the reddening E_{B-V}, the neutral hydrogen, and the Na I column densities (Herbig 1993; Friedman et al. 2011). λ5780 is well-correlated with the column density of neutral hydrogen N(H); also, for Galactic sightlines that are not in high radiation environments, the DIB correlation with N(H) is stronger than the correlation with E_{B-V}. Therefore, it is possible to estimate N(H) based on the measurement of the equivalent width of λ5780 (Friedman et al. 2011).

There are still ambiguities about DIB carriers, for instance, the large widths of DIBs argue that the carriers could not be atoms in the gas phase. On the other hand, by observing DIB features with high resolution spectrographs, some substructures appear in DIB profiles that indicate the carriers are large gas-phase molecules (Sarre et al. 1995). In addition, DIBs react to the strength of the UV field of the local environment (Cox et al. 2006) and DIB strength varies as a function of UV radiation toward different sightlines (Vos et al. 2011). For extra-galactic sightlines, observations show that DIBs are present only on sightlines with significant UV bumps (Cox et al. 2006). Therefore, specific groups of UV-resistant molecules, such as polycyclic aromatic hydrocarbons (PAHs), fullerenes, and

carbon chains are commonly the more acceptable candidates for DIB carriers (Herbig 1995).

To further our understanding of the DIB carriers and study the physical properties of interstellar environments, it is important to study the behavior of DIBs in different ISM regions. DIB carriers have been ubiquitously detected everywhere, for instance, DIBs have been observed in the Magellanic Clouds (van Loon et al. 2013), M31 and M33 (Cordiner et al. 2008a, 2008b), and beyond the Milky Way in SN host galaxies (Cox & Patat 2008). Therefore, we study the DIB carriers within the purported hot Local Bubble and beyond it to investigate the DIB behaviors in such environment.

3. OBSERVATIONS

3.1. Spectroscopy with IDS

Observations were carried out over 35 nights on 2011 October 10–15, 2012 March 1–6, 2012 September 8–12, 2012 December 31 to 2013 January 9, and 2013 May 27 to 2013 June 2. All observations were carried out using the Intermediate Dispersion Spectrograph (IDS) at the 2.5 m Isaac Newton Telescope (INT) at the Roque de Los Muchachos in La Palma. The IDS employs a long-slit spectrograph with a set of 16 gratings and two CCDs: the blue-sensitive EEV10 CCD and the RED+2 detector, which is more sensitive in the red. Both CCDs have 4096×2048 pixels. One could achieve dispersions between 0.24 and 4 Å pixel⁻¹. The spatial scale for the EEV10 is 0″.4 and for the RED+2 is 0″.44 pixel⁻¹, and the full unvignetted slit length is 3′.3.

For our observations, we used the 235 mm camera and H1800V IDS grating for an effective resolution of 0.31 Å pixel⁻¹. H1800V was chosen since it provides a high spectral resolution that is well matched to the typical width of DIBs. We chose 5800 Å as the central wavelength, in order to cover the major λ5780, λ5797, λ5850, λ6196, and λ6203 DIBs. A 1″.1 slit yielded spectra in the 5750−6040 Å region at spectral resolutions of $R \equiv \lambda/\Delta\lambda \sim 2000$ (or a velocity resolution of $\Delta v = 150$ km s⁻¹). The DIB detection requires a high signal-to-noise ratio (S/N) of at least 100, but for the detection of very weak absorptions, like the one that was detected by Cordiner (2006) toward the nearby star μ^1Cru with a λ5780 DIB equivalent width of 4 mÅ, we need an S/N of at least 2000. The seeing varied during these observing nights from 1″.1 to 1″.9.

On each observing night, we obtained more than 60 flat field frames (quartz lamp) with exposure times of 13–15 s to correct the CCD pixel-to-pixel sensitivity variations and eliminate spurious pixels in the frames. For wavelength calibration, more than 15 arc frames (CuAr+CuNe) were taken at the beginning and the end of each observing night. A large number of bias frames were also recorded. We observed the targets with 9–25 science frames for an individual star with an exposure time between 3–400 s depending on the apparent magnitude of the stars to achieve a typical continuum S/N ∼ 2000.

Some additional steps were taken in IRAF prior to extracting the spectrum with the KPNOSLIT package. The data were processed using the CCDRED data reduction package. First, an average bias frame was produced using the IMCOMBINE task by stacking ∼100 bias frames. Then the resultant frame was subtracted to correct a number of poor but recoverable columns. To correct the CCD sensitivity pattern, we combined flat frames and produced a normalized master flat and divided each science frame by this master flat. After extracting the spectrum and calibrating the wavelength range with arc frames to increase the S/N ratio up to ∼2000, by using the SCOMBINE task, we

Table 1
The Correlations of λ5780 and λ5797 with Each Other and with Na I D₁, Na I D₂ and Ca II Equivalent Widths

	Inside the Local Bubble				Outside the Local Bubble			
	Correlation	Slope	Intersection	Reduced χ^2	Correlation	Slope	Intersection	Reduced χ^2
	λ5780 DIB							
λ5797	0.96	0.26	1.62	5.1	0.97	0.28	1.91	8.9
Na I D₂	...	...	...	...	0.81	0.38	−9.50	11.7
Na I D₁	...	...	...	...	0.84	0.43	−2.03	15.4
Ca II	0.96	1.13	4.02	15.1	0.94	0.92	5.12	22.35
	λ5797 DIB							
Na I D₂	...	...	...	...	0.80	0.11	−1.05	5.8
Na I D₁	...	...	...	...	0.84	0.25	−13.12	6.24
Ca II	0.96	0.32	0.34	4.2	0.90	0.27	5.2	12.13

Note. A distinction is made between sightlines inside and outside of the Local Bubble.
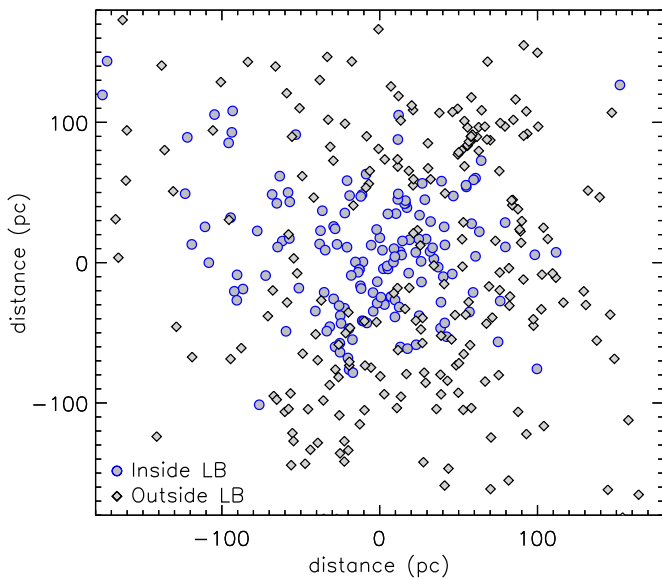
Figure 1. Projection of spatial distribution of observed stars around the Sun (map center) on the celestial equator plane. The circles are objects located inside the Local Bubble, and the diamonds show the observed targets situated outside the Local Bubble (see Section 3.2 for details).
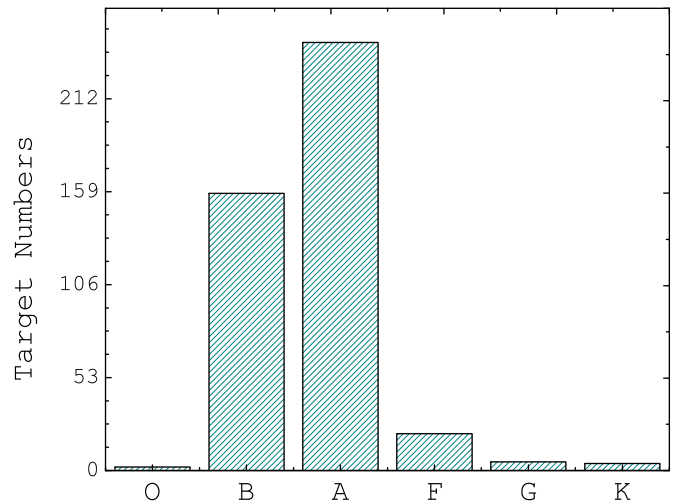

Figure 2. Histogram of observed stars spectral types. The B- and A-types represent more than 93% of the observed stars, but for more sky coverage some cooler stars were observed.

combined the science frames. The overall S/N ratio in our study is ∼2000 but, in some cases, we observed more than 25 frames, and by smoothing the spectrum by a 3 × 3 pixels box the S/N reaches ∼2800.

3.2. Target Selection

All 432 targets have been selected from the 3D Na I D lines survey of Welsh et al. (2010). The detailed list of targets are presented in Table 1 of the third paper in this series (Farhang et al. 2015). In addition, all of the selected objects have well-known distances from the *Hipparcos* satellite (Perryman et al. 1997). Since we wanted to observe the Local Bubble and its surroundings, we have selected bright stars up to a distance of 200 pc (Figure 1). To maximize the uniformity of the observed stars in the map and increase its covered density area, as well as to observe hot stars (O- and B-types) we observed some cooler stars (A, F, G, and K). As we show in Figure 2, the majority of observed stars are B- and A-types.

Since the saturation level of the IDS detector was ∼64,000 counts, a small number of targets were rejected due to their extreme brightness ($V < 1.8$ mag). To increase the observing

run efficiency, targets with $V > 7.2$ mag were also rejected from our target list to avoid very long integration times. The pointing range of the INT (zenith distance $< 70°$ and declination range $> −30°$), enabled us to observe some Southern celestial hemisphere targets; however, our targets were predominantly selected from the northern hemisphere. As shown in Figure 3 our observations cover all of the northern hemisphere. A few targets were acquired to overlap with the southern sky survey to check the consistency of the measurements.

In this paper, we perform our analysis separately for sightlines inside and outside the Local Bubble. However, given the 3D shape of the Local Bubble, a chimney-like structure, we could not divide inside and outside only based on the distance from the Sun (for example 80 pc in every direction). For selecting the stars located inside the Local Bubble, first, we select the objects with EW(Na I D₂) ⩽ 5 mÅ, because within the Local Bubble the Na I is very weak (Welsh et al. 2010). Then, according to their 3D map of Na I and Ca II, we visually identify which one is located inside the Local Bubble chimney.

4. DATA ANALYSIS

4.1. Fitting Procedure

Quantifying the equivalent widths for DIB absorption features is a real challenge in DIBs studies. In some cases, the DIB
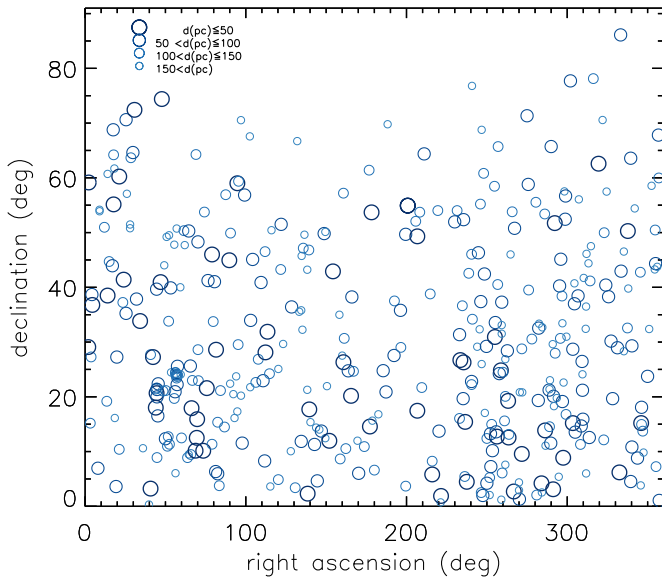
Figure 3. Observed stars in celestial coordinates. For covering all of the sky in R. A., the observations were done in six month intervals in three years.

feature is blended by that of other chemical species. Since the DIB carriers are unidentified, the shape and the width of the spectral profiles remain uncertain. Besides overlap with other species, there is a possibility for blending with features from higher rotational levels of the same species (Friedman et al. 2011). The equivalent width is defined as

$$W = \int \frac{I_0(\lambda) - I(\lambda)}{I_0(\lambda)} d\lambda = \int (1 - \exp(-\tau(\lambda))) \, d\lambda \quad (1)$$

In this equation, the I_0 and I_λ are fluxes of the continuum and the spectral line, respectively. Also, this definition shows that the EW of the line is proportional to the optical depth of the observed gas cloud $\tau(\lambda)$. For producing a normalized spectrum, continuum fitting to the observed spectra was performed by fitting a nine-order Legendre polynomial.

Since the DIB profile is inferred from an overlapping unknown number of atomic absorptions, the overall shape of the DIB profile is unknown. However, the equivalent widths, line widths, and the central velocities of the λ5780 and λ5797 lines can be approximated by a Gaussian function (e.g., van Loon et al. 2009). Therefore, we obtain the line width in terms of the σ value of the Gaussian distribution, and accordingly the FWHM is calculated as FWHM $= 2(2 \ln 2)^{1/2} \sigma = 2.355 \sigma$.

4.2. Error Estimation

The principal known source of uncertainties on DIB's EW are the blending with the stellar lines and other DIBs. One of the sources of blending contamination for λ5780 is the λ5778 DIB feature (Herbig 1975) and the probable source of blending to λ5797 is the λ5795 DIB (Krełowski et al. 1997). In the λ5780 case, because of the difference of FWHM for these two DIBs, the separation is easy but for λ5797 it is difficult (Galazutdinov et al. 2004). The corresponding statistical uncertainty for each observed DIB is computed by the standard deviation of residuals of the Gaussian fitting and summed in quadrature and weighted by the Gaussian fit (van Loon et al. 2009; Vos et al. 2011). The statistical error is always underestimated in DIB studies, since

the main source of error in the equivalent widths is the error in finding the real position of the continuum (systematic error). For computing this error, we fit three different continuum lines to the local absorption region with ±12 Å range around the central DIB wavelengths (linear fit to the continuum, quadratic fit to the continuum, and fit to DIB with linear continuum; Kos & Zwitter 2013). Accordingly, we set the intersection points of the DIB absorption and the continuum level (Krełowski & Sneden 1993), and then compute equivalent widths. Therefore, the error for systematic uncertainty is determined by the difference between the highest and lowest values of equivalent width among these three EWs.

As an example of the quality of the observed data, in Figure 4, we show some typical λ5780 and λ5797 absorptions with the best Gaussian fit line to each one. In our observations, the equivalent width of λ5780 varies between 3 and 250 mÅ but for some sightlines (e.g., HD 183143) the EW is near 800 mÅ. In our data set, the λ5797 EW varies between 3 and 150 mÅ.

4.3. Synthetic Stellar Models

Extracting interstellar spectrum features using the observations of cool star spectra containing stellar absorption lines requires a very accurate synthetic spectrum of the target star to be subtracted from the observed spectrum.

To model a stellar atmosphere, the input parameters are effective temperature $T_{\rm eff}$, surface gravity $\log g$, and microturbulence velocity ξ, which lead to the calculation of the spatial distribution of some physical quantities, such as, temperature $T(r)$, electron density $n_e(r)$, population numbers $n_i(r)$, density $\rho(r)$, velocity field $v(r)$, etc.

We calculate our atmosphere models with the ATLAS9 code, with the correction of iron and iron-peak element opacities (Kurucz 1992). We used ATLAS9 for modeling the stellar atmosphere in our samples, from Castelli & Kurucz (2003)[6] who use new Opacity Distribution Functions (ODFs) for several metallicities. We also increase spatial resolution to 72 plane parallel layers from $\log \tau_{\rm Ross} = -6.875$ to $+2$ and update all models with solar abundances (Castelli et al. 1997). For modeling each observed target atmosphere, we need the effective temperature of the observed star and the surface gravity $\log g$. We obtained these values from Cayrel et al. (1996), Varenne & Monier (1999), Reddy et al. (2003), Prugniel et al. (2007, 2011), Huang et al. (2010), and Koleva & Vazdekis (2012). Also, we determine target metallicity from Heacox (1979), Abt et al. (2002), Royer et al. (2002, 2007), and Schróder et al. (2009). After modeling the stellar atmosphere, we generate the synthetic stellar spectrum with the SYNTHE suite codes (Kurucz 2005), but we used the Linux port (Sbordone et al. 2004; Sbordone 2005). Atomic and molecular data were taken from the database on Kurucz's Web site[7] (Kurucz 2005). Also, for considering the broadening caused by rotational velocity, we use the rotational velocity from Abt et al. (2002), Royer et al. (2002, 2007), and Schróder et al. (2009), and for those stars for which the rotational velocity was not reported we use $v \sin i = 15$–$20 \, {\rm km \, s^{-1}}$. In our calculations, we included all of the atomic and molecular lines with empirically determined atomic constants plus all of the diatomic molecular lines (CH, NH, CN, MgH, SiH, SiO, H_2, C_2, and CO) except for the TiO molecule.

---

[6] http://wwwuser.oats.inaf.it/castelli/
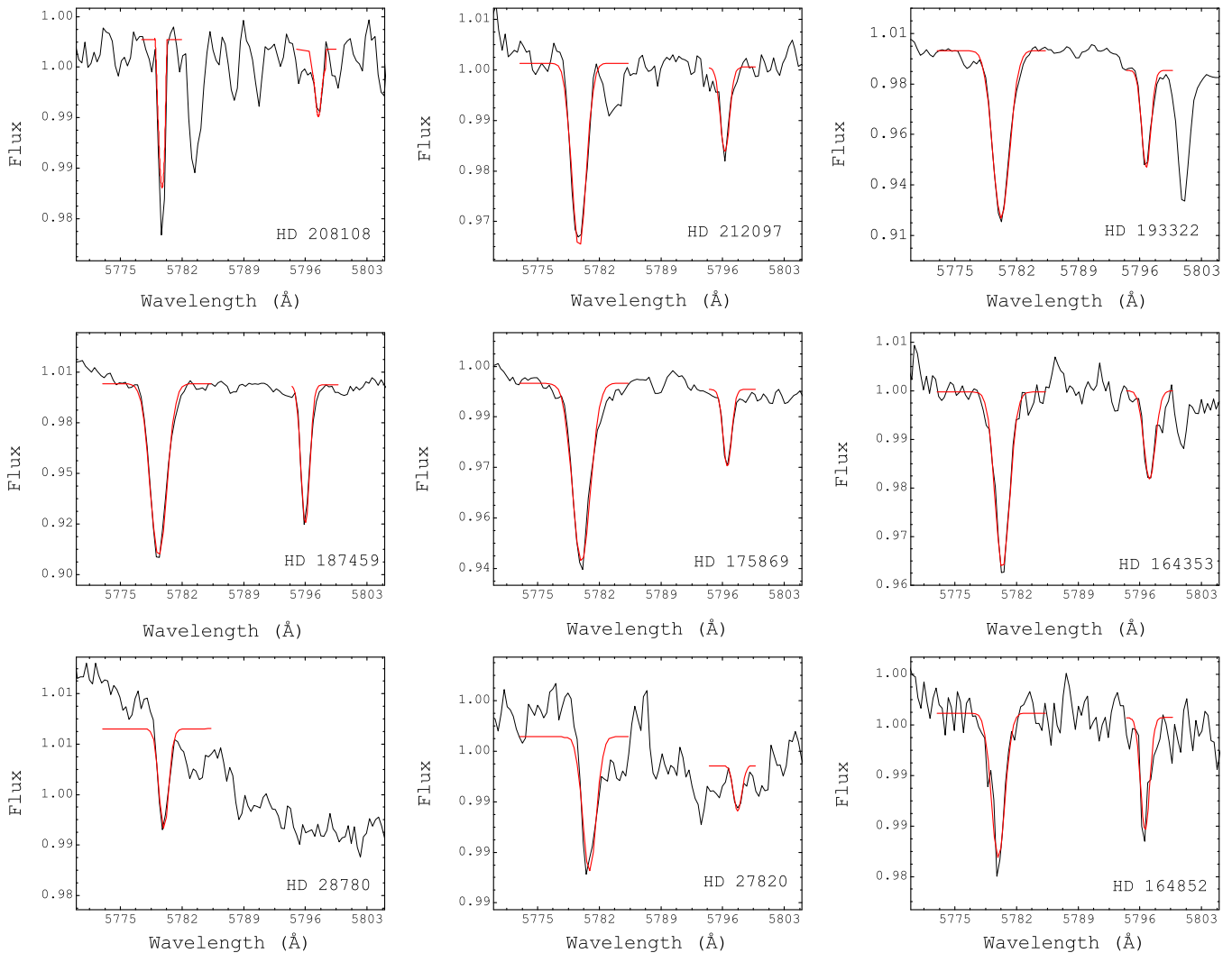[7] http://kurucz.harvard.edu

Figure 4. Some observed DIB features for quality checking. The first panel in the most upper left side (HD 208108) is an example with stellar absorptions, for which, after subtracting, a synthetic spectrum the Gaussian fit to λ5780 was done. The lower left panel (HD 28780) is a sightline with observed λ5780 and absence of λ5797 DIBs, which is common in DIB observations. The lower right panel (HD 164825) is an example with poor seeing that caused more noise than normal.

4.4. Mid-Hot Stars

For all targets, we carefully searched for the potential contaminating stellar lines. Friedman et al. (2011) showed that for late-B objects there are three Fe II stellar lines (at 5784.45 Å) that would contaminate the λ5780 DIB, but this can be easily detectable. Therefore, for our late-B type targets, we correct the λ5780 DIB absorption according to the above method. On the other hand, the main sources of A-type star contaminations at λ5780 are two strong Fe II absorptions at 5780.13 Å and 5780.37 Å and a nearby Fe II at 5783.63 Å. There is no source of contamination at λ5797.

For some observed A-type stars for which the metallicity has not been reported, we produce all possible synthetic spectra to compare with the observed spectra. The surface gravity of A-type stars varies between 3.5 and 4.2 (Gray 1992); therefore, we choose a constant $\log g = 4$ in all of the atmospheric models. From A0 to A9 spectral types, according to Theodossiou & Danezis (1991) report, we select a constant temperature for luminosity classes I, II–III, and IV–V. Also, the A-type stars have different metallicities from 0 to −2 (Beers et al. 2001). Accordingly, for a given A-type subdivision (e.g., A0) and luminosity class (e.g., IV), we produce three different atmosphere models with [Fe/H] = 0, −0.5, −1.5, and compare

with the observed spectrum to choose the best model. Also, we consider the effect of rotational velocity convolved with the instrument dispersion. However, the rotational velocities of our observed A-type stars are very high ($\sim$200 km s^{-1}) (Hoffleit & Warren 1995), thus when convolved with our instrument dispersion, the absorption lines are widened, and therefore their impact on the DIB absorption will be limited. Then, after selecting the best synthetic spectrum for an individual target, we subtract the synthetic spectrum from the observed absorption (containing both stellar and interstellar absorption features) to obtain the residual that predominantly consists of the interstellar absorption (Montes et al. 1995a, 1995b). We then fit a Gaussian function to this residual to obtain the equivalent width of the DIB (Figure 5).

4.5. Cool Stars

The presence of numerous stellar lines in a cool star's spectrum (F-, G-, and K-types) leads to an increased contamination in the interstellar absorptions and prevents an accurate determination of the EW, absorption depth, FWHM, and continuum. In these stars, the λ5780 has a two-prong fork shape (see Figure 6), which is caused by the presence of Fe II, Mn I, Si I (all near 5780.1 Å), and Cr I (5781.1 Å). Chen et al. (2013)
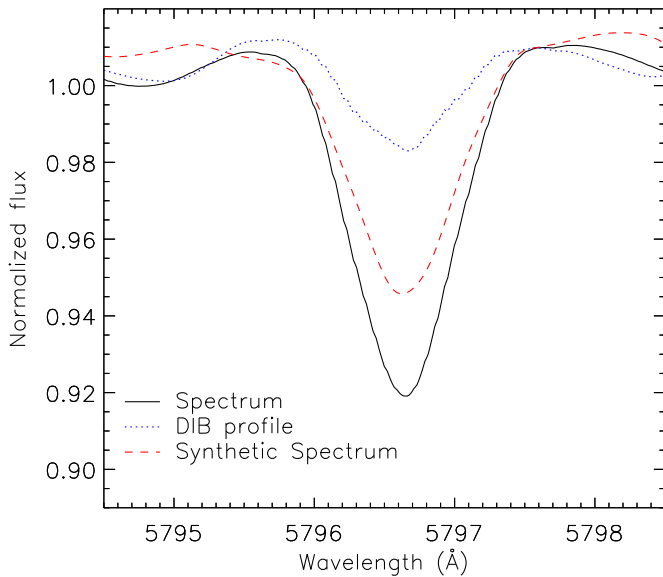
Figure 5. The black line is the observed spectrum including both stellar and interstellar absorptions, the dashed line is a synthetic stellar spectrum and the dotted line is the interstellar spectrum obtained by subtracting the synthetic spectrum from the observed one.
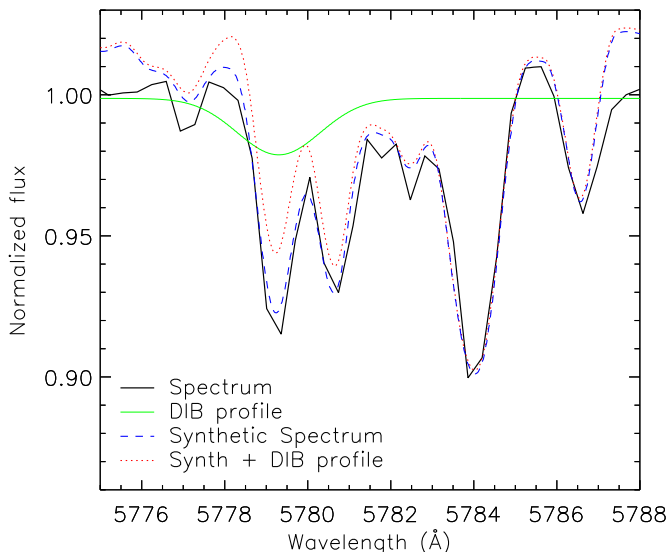

Figure 6. Spectrum of a cool star (black solid line). By changing the DIB profile parameters (thick solid line) and adding to synthetic spectrum (dotted line), the observed spectrum (dashed line) is reproduced.

studied the 6196, 6204.5, and 6283.8 Å DIBs and showed that, with the product of a synthetic stellar spectrum, a synthetic telluric transmission, and an empirical model for the DIB absorption, it would be possible to extract the spectrum of the interstellar feature. In our observations, since we focus on λ5780 and λ5797, the telluric absorptions are not considerable.

Chen et al. (2013) show that DIB transmission profiles $D(\lambda)$ can be expressed as $D(\lambda) = D_0(\lambda)^\beta$ where $D_0(\lambda)$ is a reference profile derived by high signal-to-noise observations of early-type stars. Therefore, by adjusting the β parameters, the proper profile for each DIB would be produced. According to van Loon et al. (2009), λ5780 has a Gaussian profile of

$$D(\lambda) = a \exp\left(-\frac{(\lambda - b)^2}{2\sigma}\right) + c. \tag{2}$$
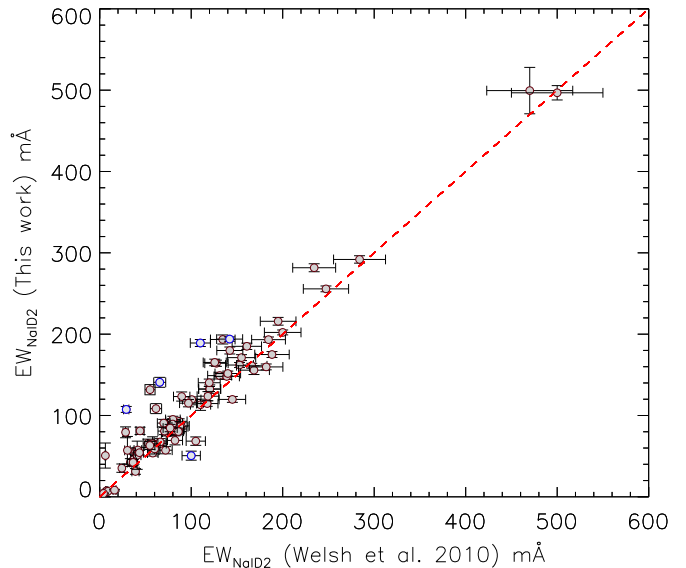

Figure 7. Comparison between Na I measurements in this work and the literature (Welsh et al. 2010). The correlation coefficient in this plot is $c = 0.97$. The most deviant objects are indicated in blue.

After confirming the average λ5780 DIB profile, according to Equation (2), in an iterative procedure, we change the a (peak intensity), b (peak center), and σ (peak width) for each wavelength (λ) to produce a new spectrum. Then, we add this spectrum to the corresponding synthetic spectrum, and in each iteration according to Equation (3), calculate the difference of the re-produced spectrum with the real observed absorption (χ^2). Eventually, the best DIB profile estimation is the one with the smallest χ^2 value.

$$\chi^2 = \sum_{i=1}^{N}\left(\frac{(F(\lambda_i) - D(\lambda_i))^2}{F_{\mathrm{err}}(\lambda_i)^2}\right) \tag{3}$$

In Figure 6, it is clear that by adding the estimated DIB profile (thick solid line) to the synthetic spectrum (dashed line), the observed spectrum (solid line) is reproduced.

Figure 7 shows a comparison between the measured Na I equivalent width in this work with Welsh et al. (2010) measurements, with a correlation coefficient $c = 0.97$. The most deviant targets (indicated by different color) in this plot are HD 200120, HD 23850, HD 24076, HD 24899, HD 48879, and HD 66824, all of which are early-type stars from B1 to A2 and are shown in Figure 8. As is clear, these targets have strong Na I absorptions and hence the deviation is most probably caused by the difference in the spectral resolution of our observations ($R = 2000$) and Welsh ($R > 50000$) data. In addition, the differences in the S/N in the sets of measurements as well as the saturation level of both surveys may well play a role as well.

5. EQUIVALENT WIDTH MEASUREMENTS

In Figure 9, we show the total equivalent width of λ5780 versus the distance from the Sun to <300 pc. Welsh et al. (2010) according to a similar plot for Na I D lines and Ca II, showed that the Na I absorption up to ∼80 pc has very low values ($W_\lambda(\mathrm{Na\,I\,D2}) < 5$ mÅ), also within ∼100 pc there is little absorption for Ca II ($W_\lambda(\mathrm{Ca\,II\,K}) < 15$ mÅ). Therefore, the volume of the Local Bubble is free of major dense interstellar
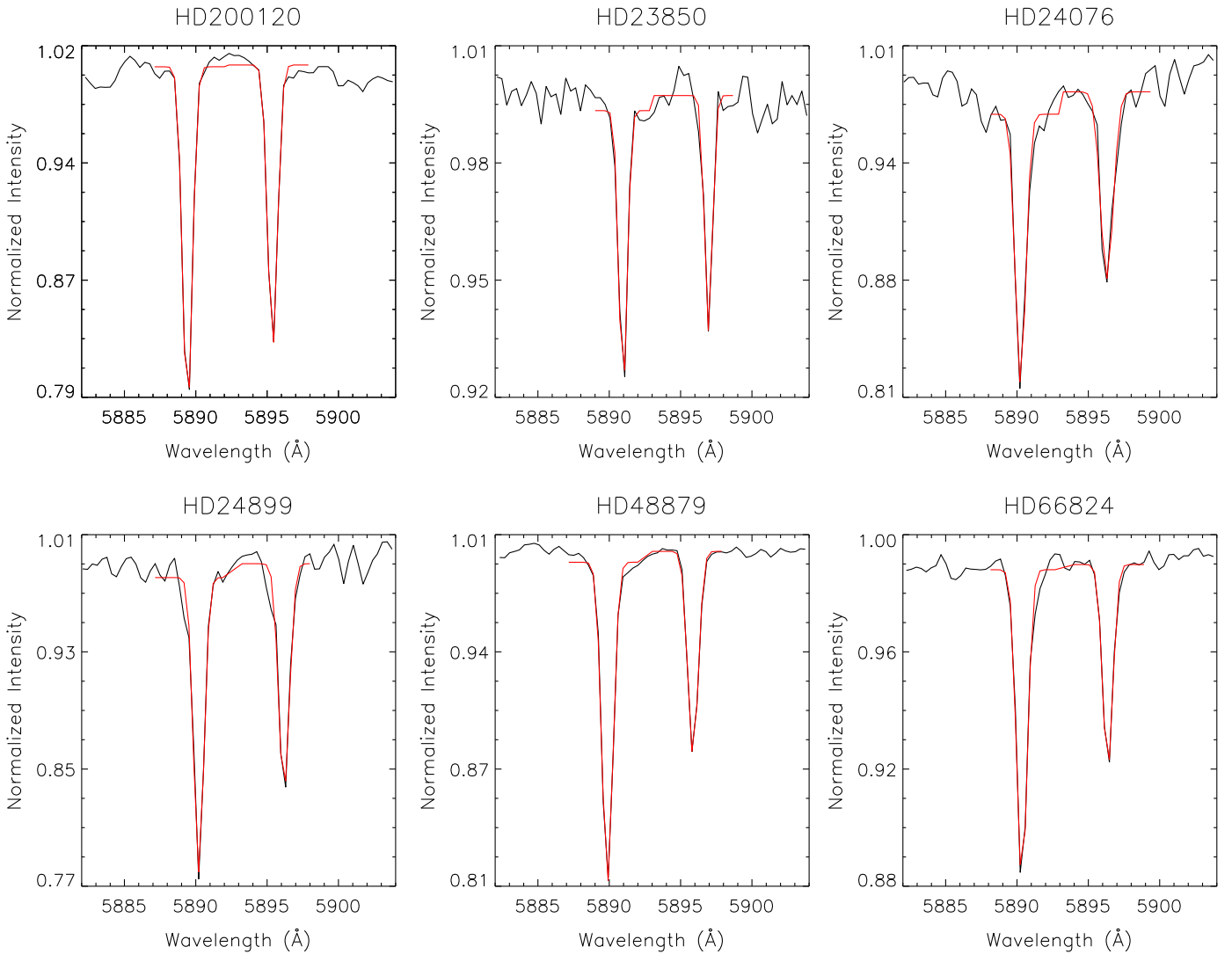
Figure 8. Most deviant objects from the Na I comparison with the literature. All of these targets are early-type stars and show strong Na I doublet absorption.
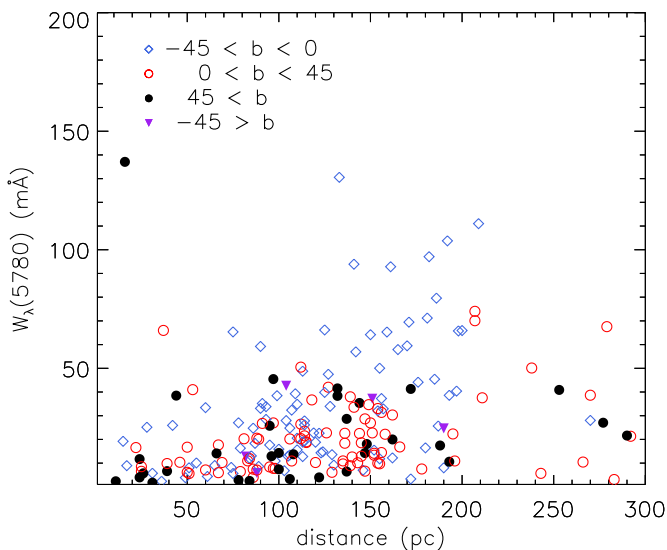

Figure 9. Equivalent width of λ5780 vs. the distance from Sun for observed targets with distances < 300 pc. Filled circles are for sightlines with $b > 45°$, red open circles are for sightlines with $b = 0$–$45°$, blue open diamonds are for sightlines with $b = 0$ to $-45°$, and filled triangles are for sightlines with $b < 45°$.

neutral gas and only has some ionized warm cloudlets of Ca II. Also, they show that beyond ~80 pc and up to ~100 pc a dense "wall" of neutral gas surrounds the Local Bubble and the value of W_λ(Ca II K) increases slowly at this wall.

In contrast with neutral and ionized gas within the Local Bubble, in Figure 9, we show that up to ~85 pc there is a fair amount of DIB absorption ($W_{\lambda5780} > 15$ mÅ). The presence of this absorption shows that within the Local Bubble, DIB cloudlets exist. However, there are several Galactic directions under the Galactic Plane (blue open diamond) with distances > 100 pc, which have strong DIB absorption. Also for Galactic directions, which are located above the Galactic Plane (red open circles), there are some sightlines with strong DIB absorption at distances > 200 pc extending into the Galactic halo through the openings of the Local Chimney (Lallement et al. 2003). The nearest stars with distances less than 80 pc that have anomalously high values of DIB absorption are HD 120136 (16 pc), HD 159332 (37 pc), HD 140436 (44 pc), HD 76756 (53 pc), HD 6658 (60 pc), and HD 218200 (75 pc).

In Figure 10, we present the plot of λ5797 absorptions versus distance from the Sun, which shows that for several sightlines located within the Local Bubble up to ~90 pc, the λ5797 absorption is strong ($W_{\lambda5797} > 15$ mÅ), and beyond the
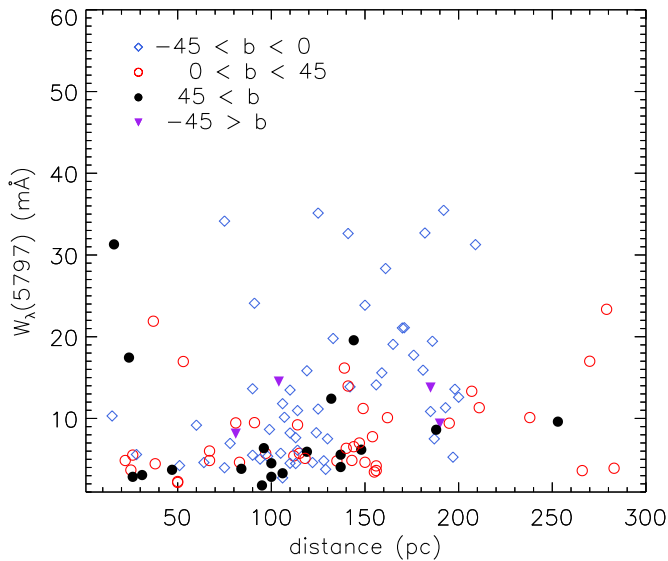
Figure 10. Equivalent width of $\lambda5797$ vs. distance from the Sun for observed targets with distances < 300 pc. Filled circles are for sightlines with $b > 45°$, red open circles are for sightlines with $b = 0$ to $45°$, blue open diamonds are for sightlines with $b = 0$ to $-45°$, and filled triangles are for sightlines with $b < 45°$.

Local Bubble's wall, the majority of $\lambda5797$ equivalent widths are $W_{\lambda5797} < 25$ mÅ. Also for sightlines located in the Galactic Halo with distances > 200 pc, which are within the Local Chimney (red open circles), the $\lambda5797$ strength is $W_{\lambda5797} < 15$ mÅ. The two nearest stars within the Local Bubble with abnormal DIB strengths ($W_{\lambda5797} > 30$ mÅ) are HD 120136 (16 pc) and HD 218200 (75 pc).

In Figure 11, we show the $\lambda5780$ equivalent width ratio to Na I D lines and Ca II. Since the Local Bubble is depleted from Na I D_1 and Na I D_2 the $W_\lambda(5780)/W_\lambda(\text{Na I } D_1)$ and $W_\lambda(5780)/W_\lambda(\text{Na I } D_2)$ can also have high values below ~80 pc, however, the ratio falls beyond 80 pc. Meanwhile, there is no significant change in the $W_\lambda(5780)/W_\lambda(\text{Ca II})$ ratio within and beyond 80 pc. The difference between the $W_\lambda(5780)/W_\lambda(\text{Na I } D)$ ratio and $W_\lambda(5780)/W_\lambda(\text{Ca II})$ within and beyond the Local Bubble indicates that the $\lambda5780$ is more associated with Na I than Ca II. This will be discussed further in Section 7.3. The rapid Na I ratio falls at the Local Bubble boundary because of the presence of dense Na I clouds around the Local Bubble which cause an increase in the equivalent width of both Na I D lines; therefore, the possibility of DIB existence increases as well. Also, high values of Ca II beyond 80 pc show that the Ca II density does not follow the density of the Na I (Welsh et al. 2010).

6. UV RADIATION AND DIB RATIO

The UV radiation has a substantial effect on DIB carriers, for instance, Krełowski et al. (1992) showed that the regions shielded from the UV radiation often have different ratios between equivalent widths of $\lambda5780$ and $\lambda5797$. UV shielded sightlines are those lines of sight that pass through the innermost regions of dense clouds, and following the observations of ζ Oph are named ζ-type clouds. However, the sightlines passing through the outer layers of clouds are nonshielded from UV radiation, and following σ Sco observations are named σ-type clouds (Krełowski & Sneden 1994). Sonnentrucker et al. (1997) concluded that the $\lambda5780$ and $\lambda5797$ DIBs are separate gas-phase molecules. By comparing W_λ/E_{B-V} as a function of E_{B-V}
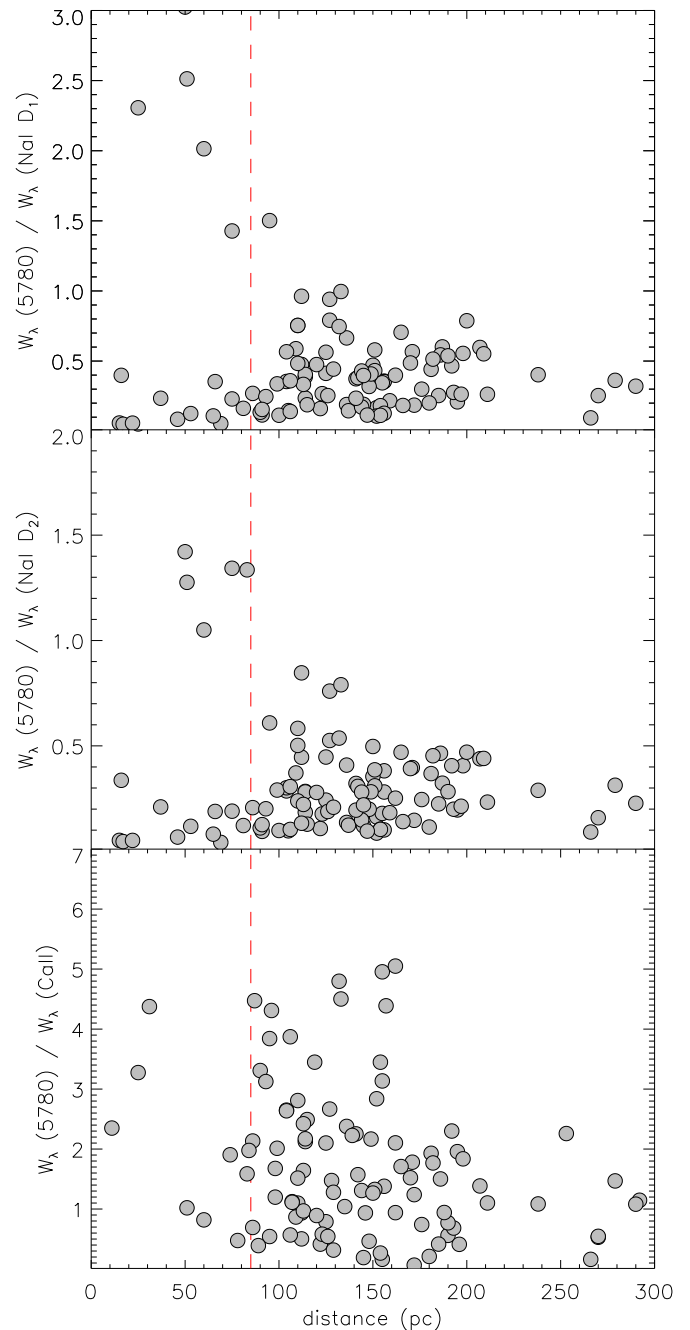

Figure 11. Equivalent width of $\lambda5780$ to atomic lines ratio. The upper panel is $W_\lambda(5780)/W_\lambda(\text{Na I } D_1)$ line. The middle panel is the $W_\lambda(5780)/W_\lambda(\text{Na I } D_2)$. The lower panel is the $W_\lambda(5780)/W_\lambda(\text{Ca II})$. The dashed line in all three panels is the d 80 pc boundary as a rough indication of the Local Bubble frontier.

for each DIB, they found that $\lambda5780$ reaches its maximum at the lowest value of E_{B-V}, indicating that the carriers of this DIBs are the most resistant of DIBs to strong UV radiation (so is the $\lambda4429$ DIB, see, e.g., van Loon et al. 2013).

However, in more UV protected denser regions (ζ-type), the $\lambda5797$ has a greater strength and the $\lambda5780$ carrier is less efficiently ionized in these regions (Vos et al. 2011). Therefore, in regions with high UV intensity, the $\lambda5780$ reaches its maximum abundance while the $\lambda5797$ carriers are ionized and then destroyed (Cami et al. 1997). As a result, this suggests that the formation of the $\lambda5780$ carriers requires UV photons. Also, since the $\lambda5797$ has a positive correlation with the overall
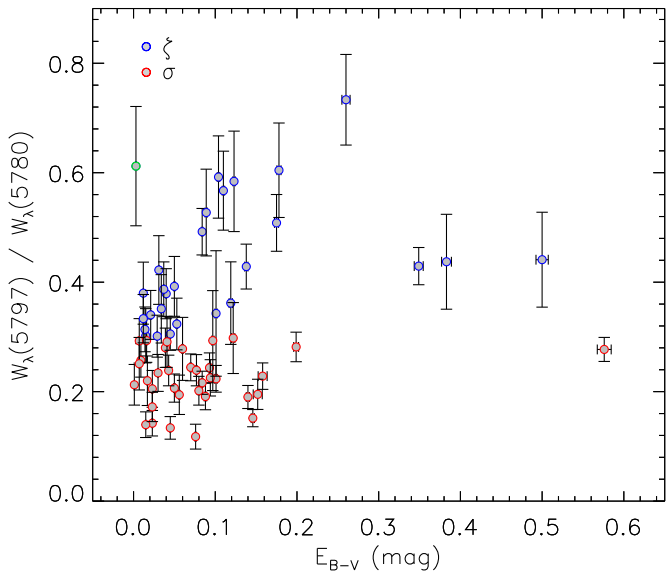
Figure 12. $W_\lambda(5797)/W_\lambda(5780)$ ratio plotted against E_{B-V}. The distribution peaks at an E_{B-V} of ~0.14 mag, indicating the optimal condition for $\lambda 5780$ formation.

Figure 13. $W_\lambda(5797)/W_\lambda(5780)$ ratio plotted against $W_\lambda(Na\,I\,D_2)/W_\lambda(Ca\,II)$. The two most scattered targets are identified in blue.

slope of the extinction curve and anticorrelates with the UV radiation, the formation of the $\lambda 5797$ carrier would benefit from the UV shielding (Megier et al. 2005). Consequently, the abundance ratio between $\lambda 5780$ and $\lambda 5797$, to some extent traces the ionization state of the DIB carriers (Vos et al. 2011).

The original definition of these two types of clouds is based on the ratio of central depths of the $\lambda 5797$ and $\lambda 5780$ DIB absorptions ($A5797/A5780 = 0.4$), which corresponds to the equivalent width ratio, $W_\lambda(5797)/W_\lambda(5780) \simeq 0.3$. Since there is a smooth transition, the exact boundary is not very important (Kos & Zwitter 2013; Vos et al. 2011).

In Figure 12, we show the $W_\lambda(5797)/W_\lambda(5780)$ ratio for observed ζ-type and σ-type clouds versus reddening. For sightlines with very low $E_{B-V} < 0.1$ mag, the σ-type clouds are sufficiently abundant, which shows that the $\lambda 5780$ carrier is more abundant than the $\lambda 5797$ carrier. The peak around $E_{B-V} \sim 0.14$ mag corresponds to sufficient shielding, and thus is the most optimal condition for the existence of the $\lambda 5797$ carrier, and instead there is insufficient UV flux to transform the $\lambda 5780$ carrier into its ionic form (Vos et al. 2011). For sightlines with $E_{B-V} > 0.25$ mag (with sufficient UV protection), the condition for the formation of the $\lambda 5797$ carriers is more favorable than in the σ sightlines. However, after $E_{B-V} > 0.25$ mag, there is no more increase in ζ-type clouds, because either the $\lambda 5797$ carrier is depleted at high densities and/or these are simply caused by superpositions of clouds with individually lower reddening. The target with a different color (green) is HD 222602, an early-type star on the main sequence with a very low color index ($B - V = +0.1$ mag). This star exhibits very strong $\lambda 5780$ and $\lambda 5797$ absorption in a high-quality spectrum.

In Figure 13, we plot the $W_\lambda(5797)/W_\lambda(5780)$ versus $W_\lambda(Na\,I\,D_2)/W_\lambda(Ca\,II)$, which shows that when the $W_\lambda(5797)/W_\lambda(5780)$ increases the $W_\lambda(Na\,I\,D_2)/W_\lambda(Ca\,II)$ increases as well. In other words, the $\lambda 5797$ carrier is associated with regions that have higher Na I absorption, probably in the dense cores of clouds. Also, in environments where the Ca II is strong, the DIBs ratio is weak, meaning that the $\lambda 5780$ strength is high or/and the $\lambda 5797$ is significantly weak. The most deviant measurements are for HD 151525, HD 164577, and HD 25642,
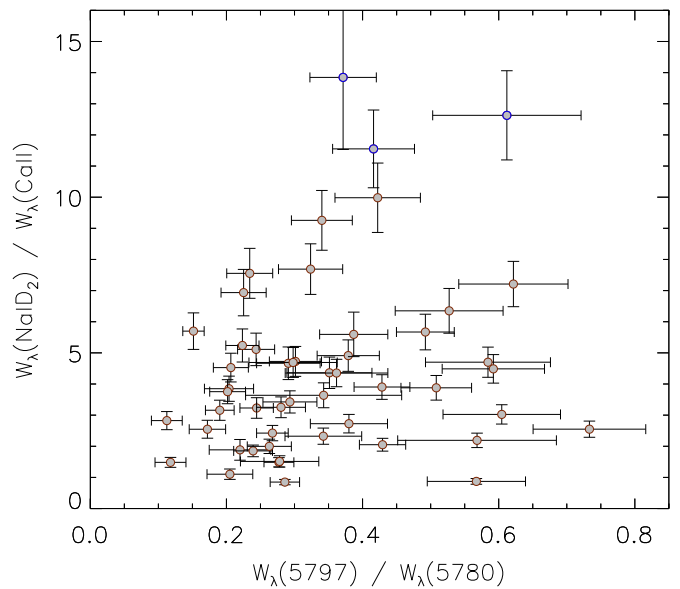
which all have a very good quality and high S/N ratio, but all sightlines have high $W_\lambda(Na\,I\,D_2)/W_\lambda(Ca\,II)$ ratios.

7. CORRELATIONS OF DIB FEATURES

7.1. Correlation between DIBs and Extinction

The DIBs are correlated well with visual reddening E_{B-V} and among all known DIBs, the $\lambda 5780$ has the strongest correlation (Herbig 1995). Megier et al. (2005) studied the DIB correlations with the slope of the extinction curve between the far-UV and other parts of the extinction curve, and also the DIB correlation with the 2175 Å bump strength. They found that among all DIBs, the $\lambda 5780$ has the strongest correlation with the bump, which could be interpreted as both the bump and the DIB carriers being composed of similar materials. There is a loose correlation between the 2175 Å bump and the extinction excess in the far-UV, which suggests that the absorbers might be carbonaceous molecules such as PAHs, particularly ionized species. Also, other identifications have been proposed for DIB carriers such as fullerenes.[8]

The DIB strengths could reflect changes in grain properties, for instance, in some directions (e.g., Sco−Oph) the slope of the reddening law ($R = A_V/E_{B-V}$) departs from the standard value.[9] Such variations in R are believed to be due to differences in the mean size of the grains in those sightlines. However, Herbig (1993) showed that DIB strengths per unit color excess do not follow the R variations, so this provides a reason to doubt whether the grains themselves can be hosts of the carriers.

To investigate the DIB correlation with visual reddening, we divide our data into two different groups. All correlation coefficients are computed for sightlines for which the star resides inside the Local Bubble and those in which the target star is outside the Local Bubble. In this study, the Johnson UBV data were taken from Kharchenko et al. (2004), Gontcharov (2006), and Kharchenko & Scholz (2007), and the stellar types

---

[8] Fullerenes are spherical or elliptical shells formed with hexagonal and pentagonal aromatic cycles like C_{60}.
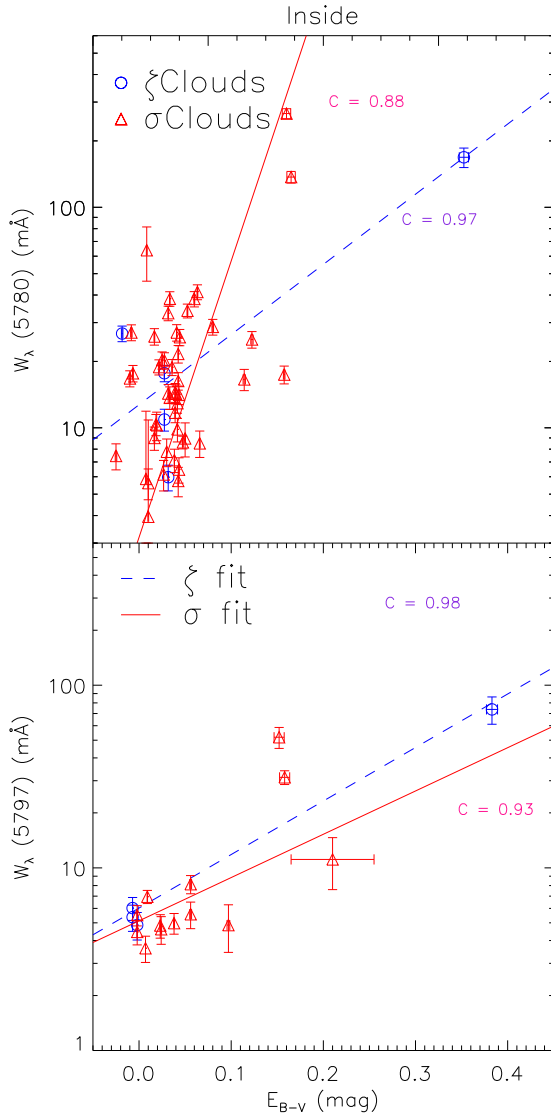[9] The overall value is $R = 3.1$ but in Sco−Oph varies between $R = 4$–4.4 (Cardelli et al. 1989).

Figure 14. Equivalent width of $\lambda 5780$ (upper panel) and $\lambda 5797$ (lower panel) vs. reddening E_{B-V} for sightlines located inside the Local Bubble. All sightlines are divided in two different σ and ζ sightlines. The triangles are σ clouds and circles are ζ clouds. Also, the dashed line is the best-fit line to ζ sightlines and the dot–dashed line is the best-fit to σ clouds. The correlation coefficients are given by c.

Figure 15. Same as Figure 14, but for outside the Local Bubble.

were selected from Hoffleit & Warren (1995). In addition, the $(B-V)_0$ intrinsic colors were taken from Fitzgerald (1968). For extracting reddening errors, we follow the method of Friedman et al. (2011), which results in E_{B-V} errors of 0.03 mag.

In Figure 14, we show the $\lambda 5780$ and $\lambda 5797$ correlation with E_{B-V} in σ-type and ζ-type clouds inside the Local Bubble. This classification reduces the scatter and improves the relation between DIB strength and reddening. As Figure 14 shows, the $\lambda 5780$ and reddening show a stronger correlation for ζ sightlines compared to σ sightlines. Although the scatter at the lower end of the relations is large, it appears that the slope of the relation for the σ-type clouds is steeper than the same for ζ-type clouds for $\lambda 5780$, indicating the $\lambda 5780$ carriers are located in low density regions of clouds. In the presence of UV radiation, the rate of molecule dissociation increases and the ionic compounds separate or split into smaller particles; also, the clouds within σ environments may have the denser, dustier cores that would result in an increased reddening. Kos & Zwitter (2013) showed
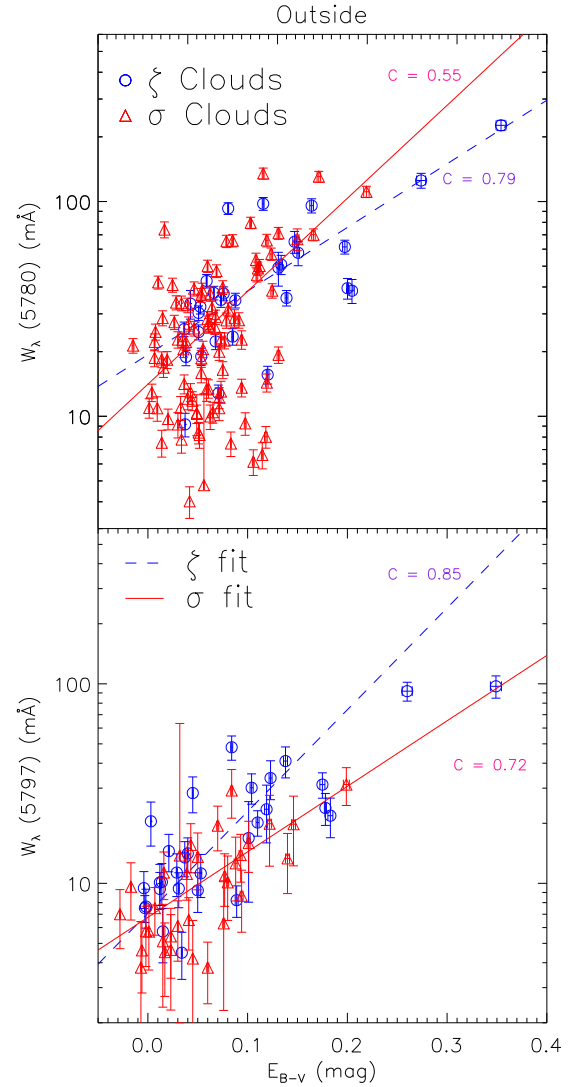
that the linear relation between the extinction and $\lambda 5797$ EW for ζ-type clouds is significantly steeper than the relation for σ sightlines, which indicates that the $\lambda 5797$ is associated with denser parts of clouds. As the lower panel of Figure 14 shows, the best fit line through $\lambda 5797$ and E_{B-V} is steeper in ζ-type clouds, which implies that the $\lambda 5797$ is located in denser parts of clouds, protected from UV radiation. A stronger correlation between the $\lambda 5780$ and $\lambda 5797$ and the reddening for ζ-type clouds, in both panels, is natural as there may be more dust in dense regions of the clouds.

In Figure 15, we show the ζ-type and σ-type clouds outside the Local Bubble for both $\lambda 5780$ and $\lambda 5797$. Both correlations for σ- and ζ-type clouds are high, but the ζ-types seem to have stronger correlations than the σ-type clouds. However, based on these data, this does not appear to be convincing. In the upper panel, the σ-type clouds show a steeper linear relation between E_{B-V} and $\lambda 5780$, which indicates that $\lambda 5780$ grows in the edges of clouds. Also, in the lower panel, the $\lambda 5797$ and E_{B-V} correlation outside the Local Bubble is steeper for ζ-type clouds, caused by the presence of the $\lambda 5797$ DIBs in the denser parts of clouds that are protected from UV radiation.

Within the Local Bubble HD 214994, HD 204862, and HD 140436 are most deviant from the best-fit line. These stars
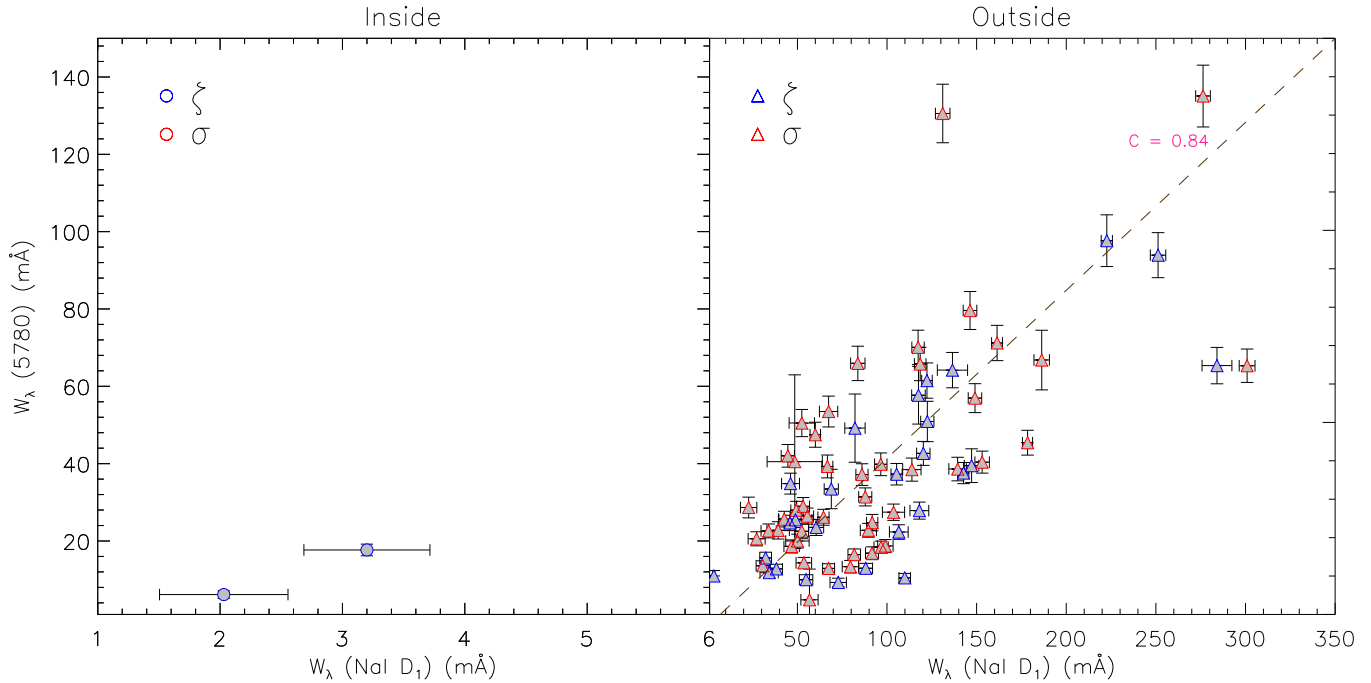
Figure 16. Correlation between the $\lambda 5780$ and Na I D_1. Left panel: within the Local Bubble. Right panel: outside of the Local Bubble. The dashed line is the best-fit line and the correlation coefficient is given by c.

have strong $\lambda 5780$ absorptions and are situated within a region with low reddening. Also, HD 18055, located beyond the Local Bubble, has strong $\lambda 5780$ absorption while it resides in a low dust region. Similarly, the most deviant targets in $\lambda 5797$ versus $E_{\rm B-V}$ outside the Local Bubble are HD 140728, HD 18484, HD 20809, and HD 23016, which have strong $\lambda 5797$ absorptions with high S/N ratio.

7.2. Correlation between DIBs and Na I

Herbig (1993) showed that the log $W(5780)$ and log $W(5797)$ follow a linear dependence on log $N(\text{Na I})$, but with a lot of scatter. He noted that the existence of these correlations with neutral atoms does not imply that the DIB carriers are neutral molecules, since if approximately the degree of first ionization was constant, equal correlations would probably be found for the ions.

In Figure 16, we plot the $\lambda 5780$ correlation with neutral Na I D_1.[10] As is shown in the figure, the targets with measurable $\lambda 5780$ values within the Local Bubble are very low in numbers, this is because of the depletion of Na I D_1 from within the Local Bubble. Therefore, it is hard to speak about correlations and linear relations. The $\lambda 5780$ and Na I D_1 correlation for the outside sightlines is clear ($c = 0.84$). In general, the existence of a common correlation between DIBs and Na I D_1 in dense clouds does not imply that DIB carriers have physical similarities to Na; rather, it shows that in each environment where the density increases the DIB strength increases as well. Likewise, we find a correlation between $\lambda 5780$ and Na I D_2 outside the Local Bubble (Figure 17). Outside the Local Bubble, HD 22091, HD 218200, and HD 27820 are most deviant from the best-fit line. In these sightlines, the Na I absorptions are strong, but the $\lambda 5780$ features are weak.

In Figure 18, we show the $\lambda 5797$ strength versus Na I D_1. Outside the Local Bubble, $\lambda 5797$ has a common correlation with the D_1 line ($c = 0.84$). If we consider $\lambda 5797$ with Na I D_2, there is a similar manner of correlation inside the Local Bubble (Figure 19). Despite the lack of data inside the Local Bubble, they are all located in ζ-type clouds and hence are in the denser parts of clouds. Again, outside the Local Bubble, there is a common correlation between $\lambda 5797$ and Na I D_2 ($c = 0.80$).

HD 42088, HD 20809, and HD 22091 are deviant from the $\lambda 5797$ and Na I D_1 linear fits outside the Local Bubble. The two first targets are located above the best-fit line, but the HD 22091 target is seen through dense Na I clouds, while its $\lambda 5797$ absorptions is weak. Likewise, HD 23016, HD 25940, and HD 22091 are deviant from the linear fit through $\lambda 5797$ and Na I D_2, such that the HD 23016 and HD 25940 are above the best-fit line, and the HD 22091 has strong Na I absorptions and weak $\lambda 5797$.

7.3. Correlation between DIBs and Ca II

We use a Ca II K-line (3393 Å) catalog (Welsh et al. 2010) to investigate the existence of possible correlations between the DIBs and Ca$^+$. This could provide information on the energy levels that are responsible for the existence, excitation, and ionization of the carriers (Galazutdinov et al. 2004). Some nearby early A-type stars have circumstellar Ca II lines, caused by the debris disks around these young stars. These Ca II lines may easily be confused with interstellar Ca II absorption (Montgomery & Welsh 2012). Because circumstellar Ca II can only be identified by repeated observation and not in a single observation, some of the Ca II measurements reported by Welsh et al. (2010) may have been affected by circumstellar absorption.

As is shown in Figure 20, the $\lambda 5780$ and Ca II correlation outside the Local Bubble is obvious, suggesting that this diffuse band is found preferentially in the same regions where Ca II forms. There is a hint of a similar trend inside the Local Bubble, but the scatter is large. The $\lambda 5797$ correlates well with Ca II
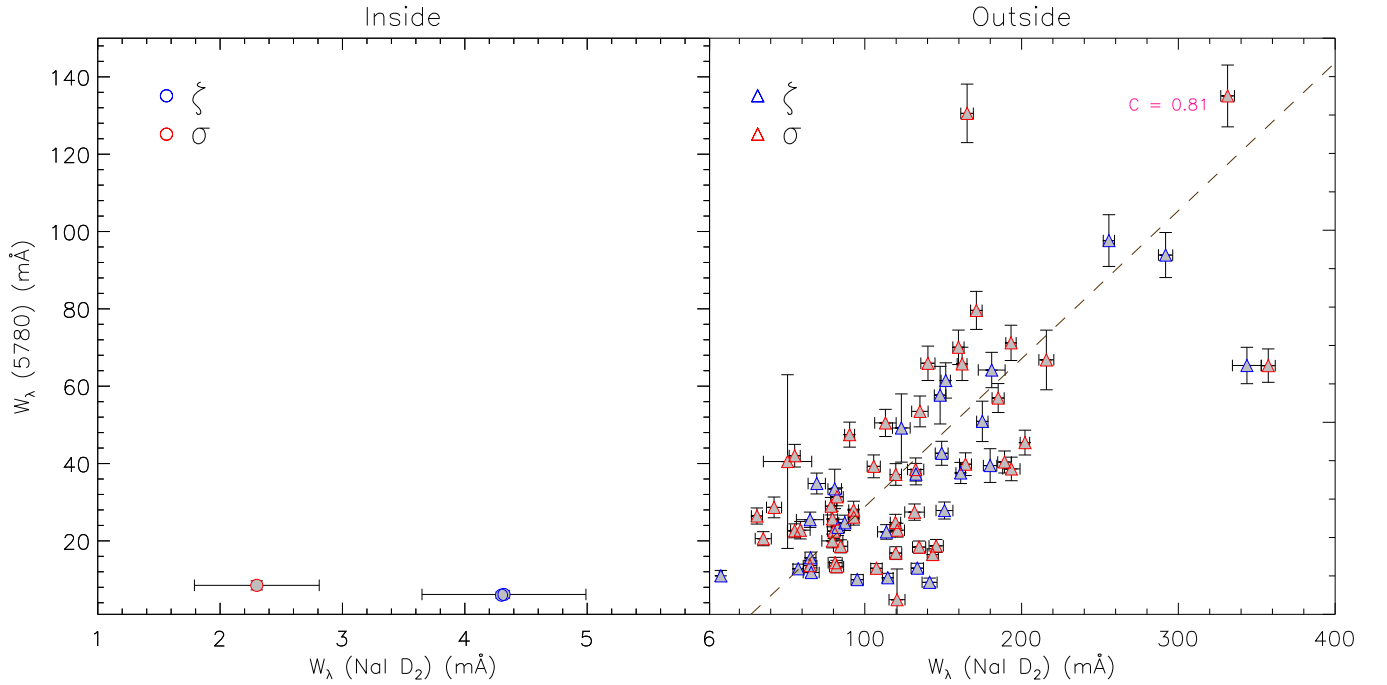
---

[10] D refers to all the transitions between the ground state and the first excited state of the Na^0 atoms and the D_1 and D_2 lines correspond to the fine-structure splitting of the excited states respectively with 5895.9 Å and 5889.9 Å.

Figure 17. Correlation between the $\lambda 5780$ and Na I D_2. Left panel: within the Local Bubble. Right panel: outside of the Local Bubble. The dashed line is the best-fit line and the correlation coefficient is given by c.
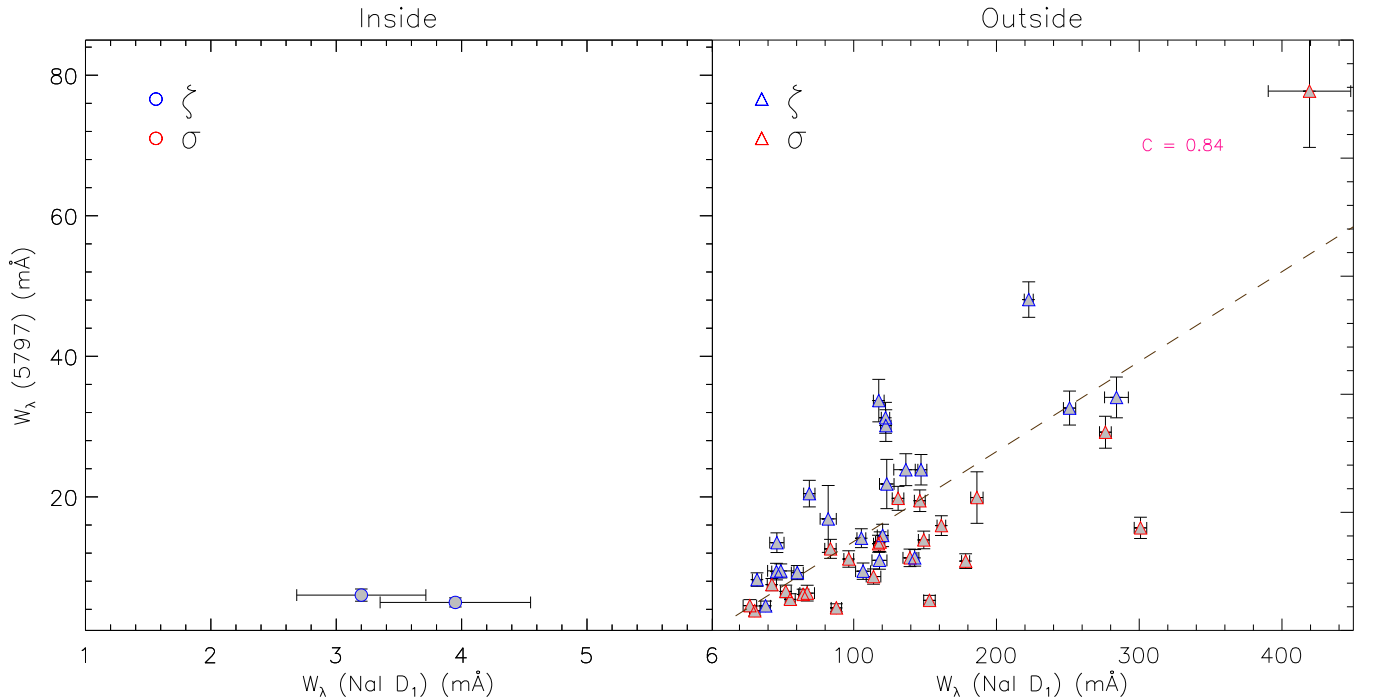

Figure 18. Correlation between the $\lambda 5797$ and Na I D_1. Left panel: within the Local Bubble. Right panel: outside of the Local Bubble. The dashed line is the best-fit line and the correlation coefficient is given by c.

outside the Local bubble, and a similar trend can be seen inside the Local Bubble (Figure 21). The correlation between Ca II with $\lambda 5780$ is stronger than its correlation with $\lambda 5797$, suggesting that $\lambda 5780$ is more associated with regions where Ca$^+$ is more abundant. Given that the Ca II appears in more radiant regions, the $\lambda 5780$ macromolecule may have an electrically charged carrier (for more discussion see van Loon et al. 2009).

Inside the Local Bubble, absorptions associated with ζ-type clouds have small Ca II values ($\leqslant 5$ mÅ), for both DIBs. This shows that the dense regions of clouds are cooler and thus

depleted from Ca II atoms. Also within the Local Bubble, in the σ-type clouds, the Ca II is more intense and the $\lambda 5780$ intensity is obviously higher than the $\lambda 5797$ values. This suggests that within the Local Bubble the σ-type clouds are dominant in the warmer mediums.

The most deviant targets from the best-fit line of Ca II and $\lambda 5780$ outside the Local Bubble are HD 216057, HD 77770, HD 220599, and 40724, which have strong Ca II absorption, but relatively weak $\lambda 5780$ feature. Also, in the direction of HD 26912, the $\lambda 5780$ absorption is strong but the Ca II located
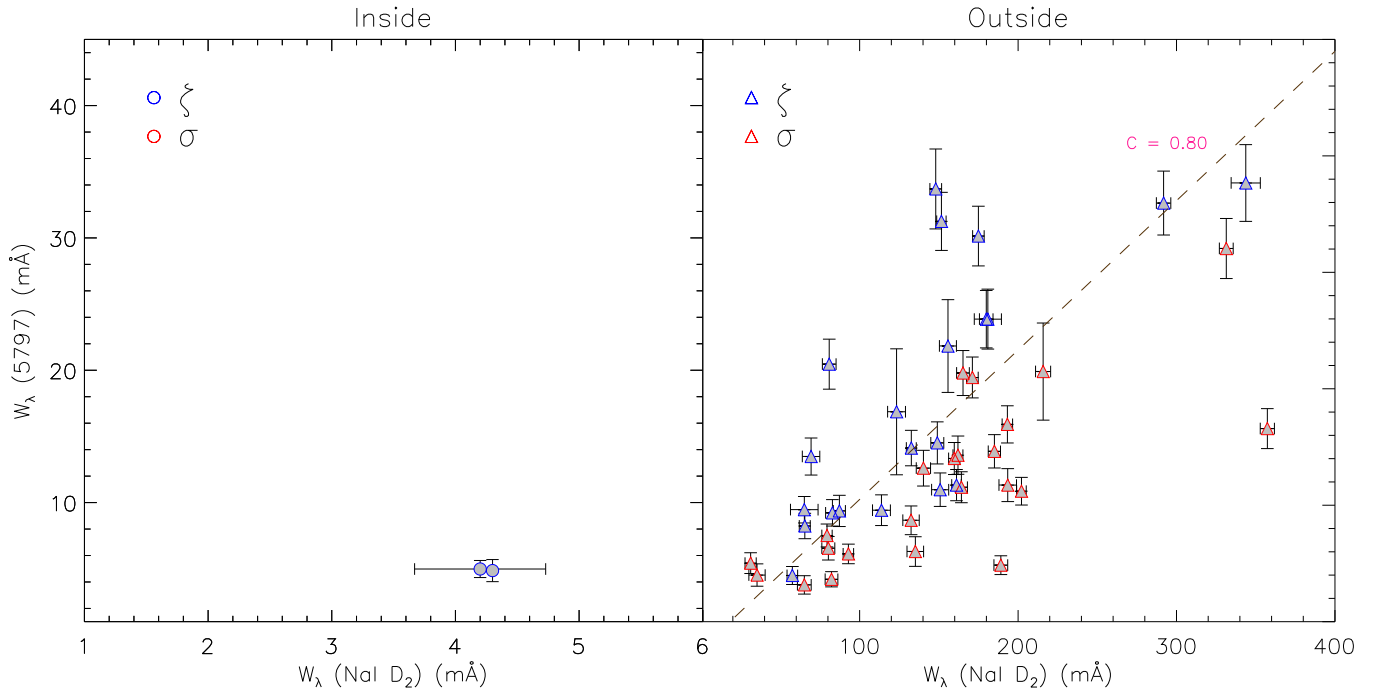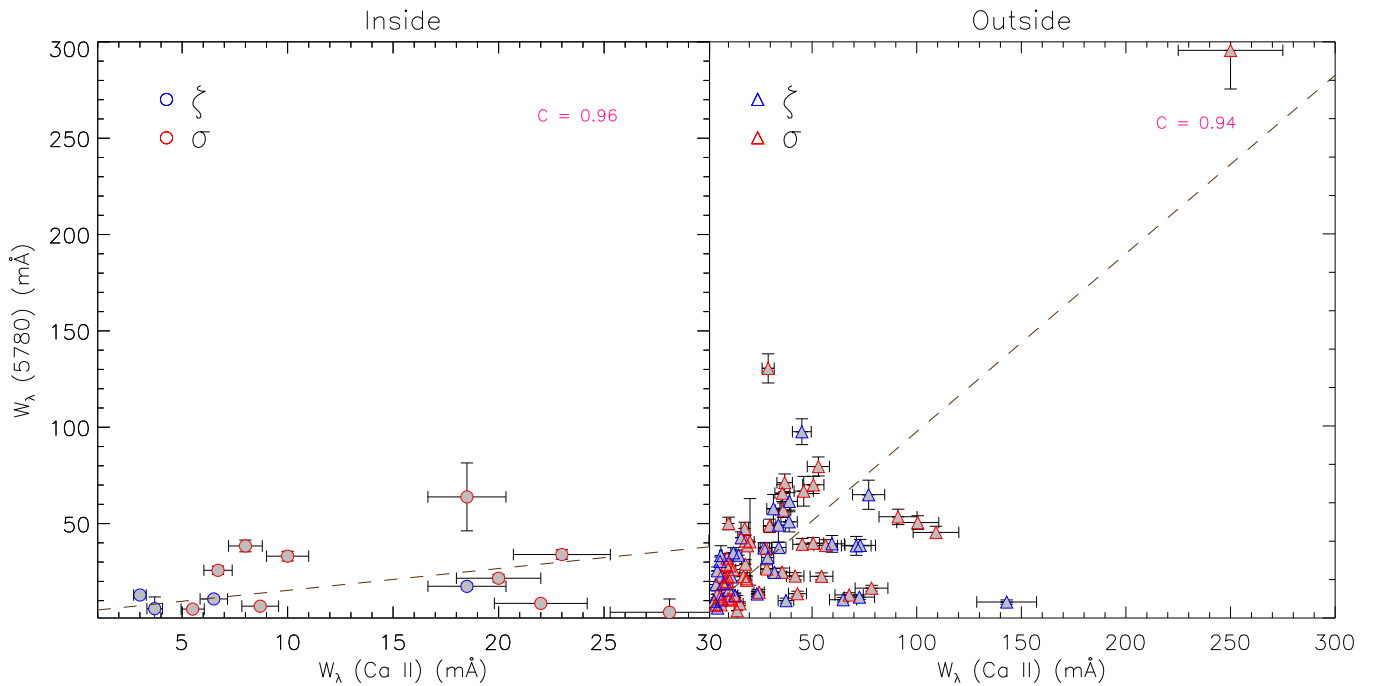
Figure 19. Correlation between the $\lambda5797$ and Na I D_2. Left panel: within the Local Bubble. Right panel: outside of the Local Bubble. The dashed line is the best-fit line and the correlation coefficient is given by c.

Figure 20. Correlation between the $\lambda5780$ and Ca II. Left panel: within the Local Bubble. Right panel: outside of the Local Bubble. The dashed line is the best-fit line and the correlation coefficient is given by c.

in this sightline is weak. For $\lambda5797$ and Ca II outside the Local Bubble, the most deviant targets are HD 216057 and HD 166182 which have strong Ca II absorptions and weak $\lambda5797$ feature. However, the HD 20809 have strong $\lambda5797$ absorption but a weak Ca II feature.

7.4. Correlation between DIBs

As shown in Figure 22, there is a fairly clear correlation between $\lambda5780$ and $\lambda5797$ both outside and inside the Local Bubble. This suggests both DIB carriers form, or are

existed, in environments that are generally found to co-exist. The scatter is larger inside the Local Bubble than outside, reflecting the more diffuse ISM within the Local Bubble and the correspondingly greater sensitivity to small variations in cloud structure.

If linear fitting between equivalent widths of two species does not pass through the origin. This may be evidence of a threshold effect such that a substantial amount of one kind must be produced before the other. Friedman et al. (2011) showed that among all DIB correlations with $\lambda5780$, only $\lambda6613.6$ and
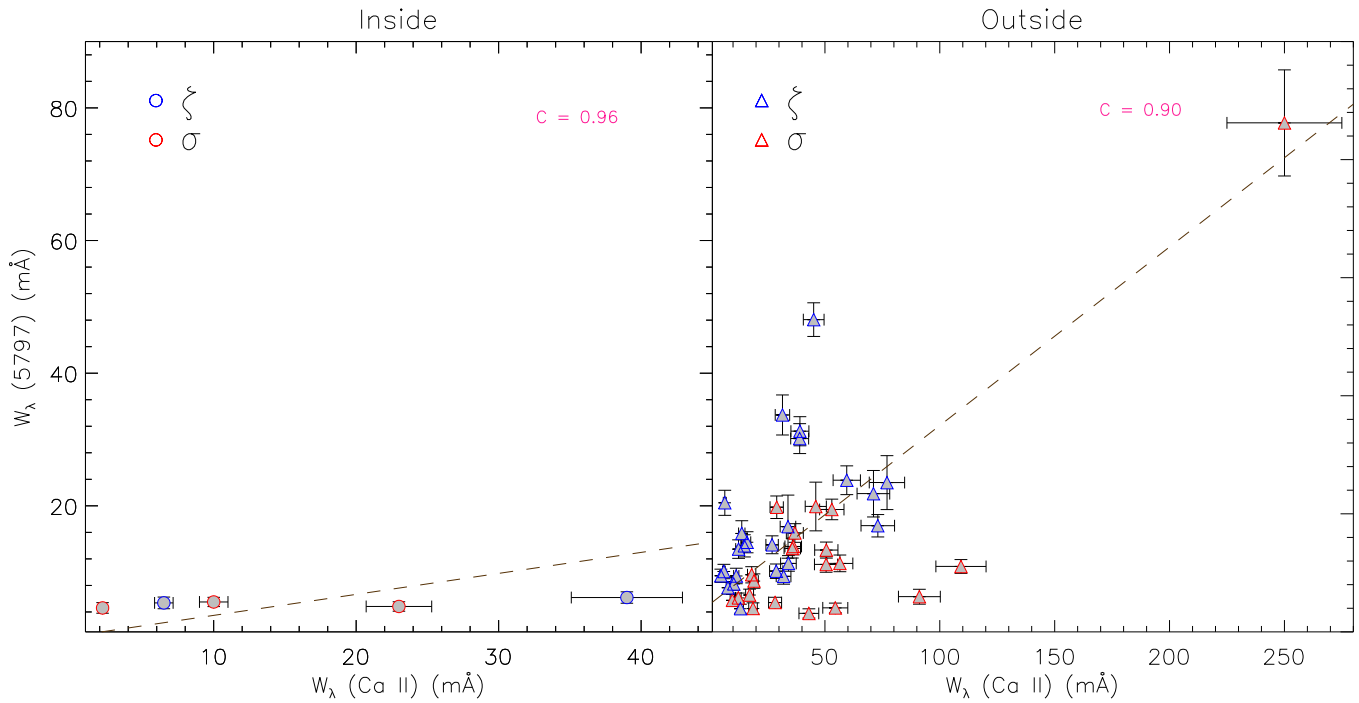
Figure 21. Correlation between the λ5797 and Ca II. Left panel: within the Local Bubble. Right panel: outside of the Local Bubble. The dashed line is the best-fit line and the correlation coefficient is given by *c*.
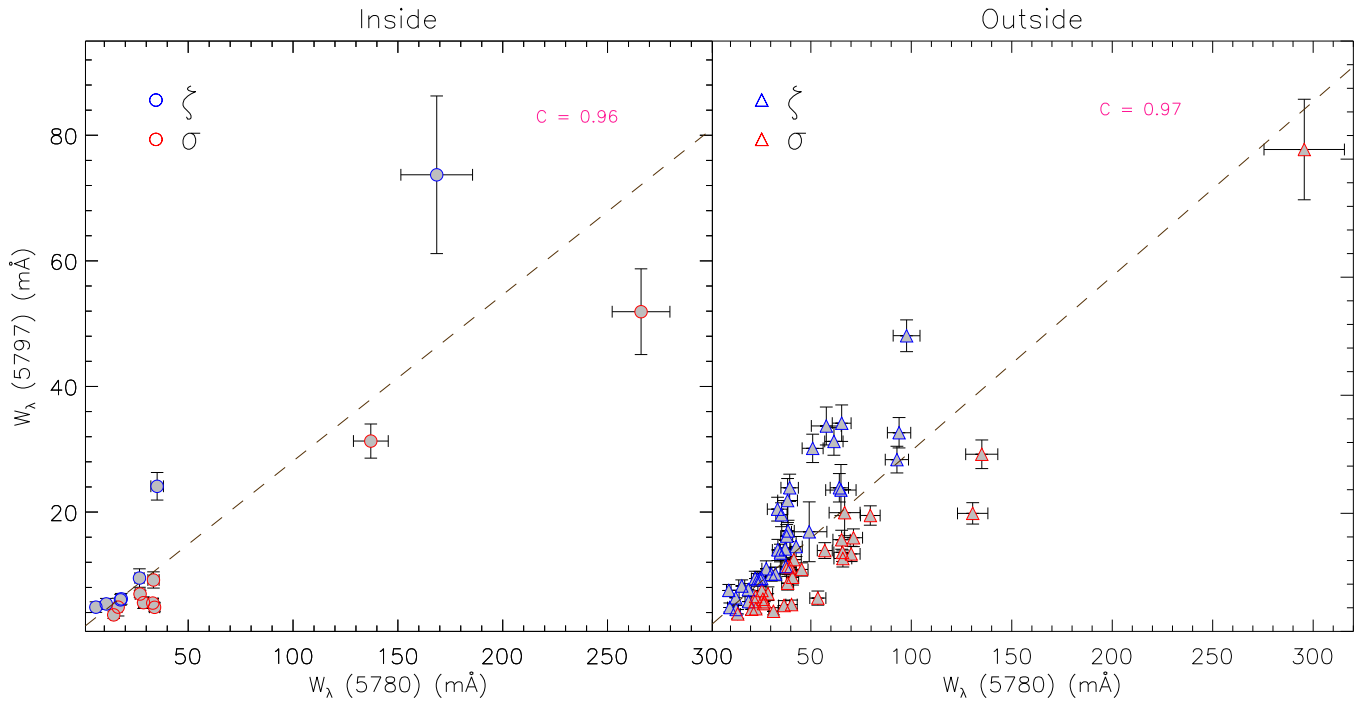

Figure 22. Correlation between the λ5780 and λ5797. Left panel: within the Local Bubble. Right panel: outside of the Local Bubble. The dashed line is the best-fit line and the correlation coefficient is given by *c*.

λ6283 have a linear fits that do not pass through the origin. They concluded that the λ5780 DIB must be produced before the λ6613.6 begins to form, and λ6283 appears before λ5780. In our observations, as shown in Table 1, similarly we find that the intercept of the linear fitting for the correlation of λ5780 and λ5797 passes through the origin. This shows that both λ5780 and λ5797 originate from one source, in and around the Local Bubble.

8. CONCLUSIONS

High signal-to-noise spectra of 432 hot stars within a distance of ∼200 pc were obtained, with the aim to study the Local Bubble and its surroundings. All observations were taken in the northern hemisphere, complementing the southern survey (Paper I). We investigate the spatial variation of the λ5780 and λ5797 strengths within and beyond the Local Bubble.

We also compare the $\lambda 5780$ and $\lambda 5797$ absorptions with interstellar reddening, Na I and Ca II. Our main conclusions are summarized as follows.

1. The $W_\lambda(5797)/W_\lambda(5780)$ ratio versus E_{B-V} indicates that the σ-type clouds are distributed around very low $E_{B-V} < 0.1$ mag. Meanwhile, since the $\lambda 5780$ is more abundant in the σ-type clouds, the peak shows that the $\lambda 5780$ tends to be present in irradiated regions with low UV shielding. Also, the ζ peak is found around $E_{B-V} \sim 0.14$ mag, which indicates sufficient UV shielding. Since the $\lambda 5797$ is more prevalent in the ζ-type clouds, the peak shows that the $\lambda 5797$ carriers grow in regions with sufficient shielding where they are protected from the background UV radiation.

2. Both inside and outside the Local Bubble, the $\lambda 5780$ and reddening relation is steeper for σ sightlines than for ζ sightlines. This suggests that in ζ sightlines the denser, dustier cores of clouds become more dominant, increasing the reddening but not leading to a similar increase in $\lambda 5780$ absorption as this DIB carrier resides in the more diffuse gas. In contrast, the $\lambda 5797$ and reddening relation is steeper in ζ sightlines because the $\lambda 5797$ carrier is more closely associated with denser parts of clouds where it is shielded from UV radiation.

3. The $W_\lambda(5797)/W_\lambda(5780)$ ratio increases with the $W_\lambda(\text{Na I } D_2)/W_\lambda(\text{Ca II})$ ratio. It is fairly established that, in the dense core of clouds the Na I and $\lambda 5797$ is more abundant and, as the cloud becomes less dense toward the outer regions of the cloud, the Na I becomes weaker and the $\lambda 5780$ DIB appears. Also, the outer regions are subject to greater irradiations and the Na I disappears and Ca II starts to dominate (van Loon et al. 2009). Therefore, when the $W_\lambda(5797)/W_\lambda(5780)$ ratio increases, it means that we are increasingly dominated by the cores of clouds that are more shielded from background UV, so the $W_\lambda(\text{Na I } D_2)/W_\lambda(\text{Ca II})$ ratio increases too.

Outside the Local Bubble, the $\lambda 5780$ and $\lambda 5797$ are well correlated with the Na I doublet lines. However, the $\lambda 5780$ correlation is stronger than the $\lambda 5797$ correlation, therefore, the sightlines outside the Local Bubble are translucent and hence the σ behavior would be expected to dominate.

The $\lambda 5780$ and $\lambda 5797$ are well correlated with Ca II outside of the Local Bubble, suggesting that these diffuse bands are found preferentially in the same areas where Ca II forms. There is a hint of a similar trend inside the Local Bubble, but with a greater scatter. van Loon et al. (2009) mentioned that the Ca II traces the warm medium. Therefore, maybe the higher correlation value for inside sightlines caused by the high temperature of Local Bubble.

REFERENCES

Abt, H. A., Levato, H., & Grosso, M. 2002, A&A, 573, 359
Bailey, M., van Loon, J. Th., et al. 2015, A&A, submitted
Beers, T. C., Rossi, S., O'Donoghue, D., et al. 2001, MNRAS, 320, 451
Bohlin, R. 1975, ApJ, 200, 402
Bowyer, C. S., Field, G. B., & Mack, J. F. 1968, Natur, 217, 32
Cami, J., Sonnentrucker, P., Ehrenfreund, P., & Foing, B. H. 1997, A&A, 326, 822
Cardelli, J. A., Clayton, G. C., & Mathis, J. S. 1989, ApJ, 345, 245
Castelli, F., Gratton, R. G., & Kurucz, R. L. 1997, A&A, 318, 841
Castelli, F., & Kurucz, R. L. 2003, in IAU Symp. 210, Modelling of Stellar Atmospheres, ed. N. Piskunov & W. W. Weiss (Uppsala: Uppsala Univ.), 20
Cayrel de Strobel, G., Soubiran, C., Friel, E. D., Ralite, N., & François, P. 1996, yCat, 3200, 0
Chen, H. C., Lallement, R., Babusiaux, R., et al. 2013, A&A, 550, A62
Cordiner, M. A. 2006, PhD thesis, Univ. Nottingham
Cordiner, M. A., Cox, N. L. J., Trundle, C., et al. 2008a, A&A, 480, 13
Cordiner, M. A., Smith, K. T., Cox, N. L. J., et al. 2008b, A&A, 492, 5
Cox, N. L. J., Cordiner, M. A., Cami, J., et al. 2006, A&A, 447, 991
Cox, N. L. J., & Patat, F. 2008, A&A, 485, 9
Crawford, I. A. 1991, A&A, 247, 183
Crawford, I. A. 2001, MNRAS, 327, 841
Farhang, A., Khosroshahi, H. G., Javadi, A., & van Loon, J. Th. 2015, ApJS, 216, 33
Fitzgerald, M. Pini 1968, ApJ, 73, 983
Friedman, S. D., York, D. G., McCall, B. J., et al. 2011, ApJ, 727, 33
Galazutdinov, G. A., Manicó, G., Pirronello, V., & Krełowski, J. 2004, MNRAS, 355, 169
Gontcharov, G. A. 2006, AstL, 32, 759
Gray, D. F. 1992, The Observation and Analysis of Stellar Photospheres (Cambridge Astrophysics Series, vol. 20, 3rd ed.; Cambridge Univ. Press)
Heacox, W. D. 1979, ApJS, 41, 675
Heger, M. L. 1922, LicOB, 337, 141
Herbig, G. H. 1975, ApJ, 196, 129
Herbig, G. H. 1993, ApJ, 407, 142
Herbig, G. H. 1995, ARA&A, 33, 19
Hobbs, L. M., York, D. G., Snow, T. P., et al. 2008, ApJ, 680, 1256-1270
Hobbs, L. M., York, D. G., Thorburn, J. A., et al. 2009, ApJ, 705, 32
Hoffleit, D., & Warren, W. H., Jr. 1995, yCat, 5050, 0
Huang, W., Gies, D. R., & McSwain, M. V. 2010, ApJ, 722, 605
Kharchenko, N. V., Piskunov, A. E., & Scholz, R.-D. 2004, AN, 325, 740
Kharchenko, N. V., & Scholz, R. D. 2007, AN, 328, 889
Koleva, M., & Vazdekis, A. 2012, A&A, 538, 143
Kos, J., & Zwitter, T. 2013, ApJ, 774, 72
Kos, J., Zwitter, T., Wyse, R., et al. 2014, Science, 345, 791
Krełowski, J., Schmidt, M. R., & Snow, T. P. 1997, PASP, 109, 1135
Krełowski, J., & Sneden, C. 1993, PASP, 105, 1141
Krełowski, J., & Sneden, C. 1994, in ASP Conf. Ser. 58, The First Symposium on the Infrared Cirrus and Diffuse Interstellar Clouds, ed. R. M. Cutri & W. B. Latter (San Francisco, CA: ASP), 12
Krełowski, J., Snow, T. P., Seab, C. G., & Papaj, J. 1992, MNRAS, 258, 693
Kurucz, R. L. 1992, RMxAA, 23, 45
Kurucz, R. L. 2005, MmSAI, 8, 14
Lallement, R., Welsh, B. Y., Vergely, J. L., et al. 2003, A&A, 411, 447
Megier, A., Krełowski, J., & Weselak, T. 2005, MNRAS, 358, 563
Merrill, P. W. 1936, ApJ, 83, 126
Montes, D., De Casto, E., Fernandes-Figueroa, M. J., & Cornide, M. 1995a, A&AS, 114, 187
Montes, D., De Casto, E., Fernandes-Figueroa, M. J., & Cornide, M. 1995b, A&AS, 109, 135
Montgomery, S. L., & Welsh, B. Y. 2012, PASP, 124, 1042
Paresce, F. 1984, AJ, 89, 1022
Perryman, M. A. C., Lindegren, L., Kovalevsky, J., et al. 1997, A&A, 323, 49
Prugniel, P., Soubiran, C., Koleva, M., & Le Borgne, D. 2007, yCat, 3251, 0
Prugniel, P., Vauglin, I., & Koleva, M. 2011, A&A, 531, A165
Puspitarini, L., Lallement, R., Vergely, J. L., & Snowden, S. L. 2014, A&A, 566, AA13
Reddy, B. E., Tomkin, J., Lambert, D. L., & Allende Prieto, C. 2003, MNRAS, 340, 304
Royer, F., Grenier, S., Baylac, M. O., Gómez, A. E., & Zorec, J. 2002, A&A, 393, 897

Royer, F., Zorec, J., & Gómez, A. E. 2007, A&A, 463, 671
Sarre, P. J., Miles, J. R., Kerr, T. H., et al. 1995, MNRAS, 277, 41
Sarre, P. J. 2006, JMoSp, 238, 1
Sbordone, L. 2005, MmSAI, 8, 61
Sbordone, L., Bonifacio, P., Castelli, F., & Kurucz, R. L. 2004, MSAIS, 5, 93
Schróder, C., Reiners, A., & Schmitt, J. H. M. M. 2009, A&A, 493, 1099-1107
Slavin, J. D. 1989, ApJ, 346, 718
Smith, L. J., & Gallagher, J. S. 2001, MNRAS, 326, 1027
Snowden, S. L., Egger, R., Finkbeiner, D., Freyberg, M., & Plucinsky, P. 1998, ApJ, 493, 715
Sonnentrucker, P., Cami, J., Ehrenfreund, P., & Foing, B. H. 1997, A&A, 327, 1215
Theodossiou, E., & Danezis, E. 1991, Ap&SS, 183, 91

van Loon, J. Th., Bailey, M., Tatton, B. L., et al. 2013, A&A, 550, 108
van Loon, J. Th., Smith, K. T., McDonald, I., et al. 2009, MNRAS, 399, 195
Varenne, O., & Monier, R. 1999, A&A, 351, 247
Vergely, J. L., Freire, F. R., Siebert, A., & Valette, B. 2001, A&A, 366, 1016
Vos, D. A. I., Cox, N. L. J., Kaper, L., Spaans, M., & Ehrenfreund, P. 2011, A&A, 533, A129
Weaver, R., McCray, R., Castor, J., Shapiro, P., & Moore, R. 1977, ApJ, 218, 377
Welsh, B. Y., Lallement, R., Vergely, J. L., & Raimond, S. 2010, A&A, 510, A54
Welsh, B. Y., & Shelton, R. L. 2009, Ap&SS, 323, 1
Weselak, T., Galazutdinov, G. A., Musaev, F. A., & Krełowski, J. 2008, A&A, 484, 381